

# Haptic Transparency and Interaction Force Control for a Lower Limb Exoskeleton

Emek Barış Küçüktabak <sup>ID</sup>, Student Member, IEEE, Yue Wen <sup>ID</sup>, Sangjoon J. Kim <sup>ID</sup>, Matthew R. Short <sup>ID</sup>, Daniel Ludvig <sup>ID</sup>, Member, IEEE, Levi Hargrove <sup>ID</sup>, Member, IEEE, Eric J. Perreault <sup>ID</sup>, Kevin M. Lynch <sup>ID</sup>, Fellow, IEEE, and José L. Pons <sup>ID</sup>, Senior Member, IEEE

**Abstract**—Controlling the interaction forces between a human and an exoskeleton is crucial for providing transparency or adjusting assistance or resistance levels. However, it is an open problem to control the interaction forces of lower limb exoskeletons designed for unrestricted overground walking. For these types of exoskeletons, it is challenging to implement force/torque sensors at every contact between the user and the exoskeleton for direct force measurement. Moreover, it is important to compensate for the exoskeleton's whole-body gravitational and dynamical forces, especially for heavy lower limb exoskeletons. Previous works either

Manuscript received 29 July 2023; revised 13 November 2023; accepted 5 January 2024. Date of publication 29 January 2024; date of current version 26 February 2024. This paper was recommended for publication by Associate Editor S. Mohammed and Editor K. Mombaur upon evaluation of the reviewers' comments. This work was supported in part by the National Science Foundation/National Robotics Initiative under Grant 2024488, in part by the Northwestern University, and in part by the Turkish Fulbright Commission. (*Corresponding author: Emek Barış Küçüktabak.*)

This work involved human subjects or animals in its research. Approval of all ethical and experimental procedures and protocols was granted by the institutional review board (IRB) of Northwestern University under Application No: STU00212684, and performed in line with the Declaration of Helsinki.

Emek Barış Küçüktabak is with the Center for Robotics and Biosystems, Department of Mechanical Engineering, Northwestern University, Evanston, IL 60208 USA, and also with the Shirley Ryan AbilityLab, Chicago, IL 60611 USA (e-mail: baris.kucuktak@gmail.com).

Yue Wen and Sangjoon J. Kim are with the Shirley Ryan AbilityLab and Department of Physical Medicine and Rehabilitation, Northwestern University, Chicago, IL 60208 USA (e-mail: yue.wen@ucf.edu; sangjoon.j.kim@gmail.com).

Matthew R. Short is with the Shirley Ryan AbilityLab and Department of Biomedical Engineering, Northwestern University, Evanston, IL 60208 USA (e-mail: mshort@u.northwestern.edu).

Daniel Ludvig is with the Department of Biomedical Engineering, Northwestern University, Chicago, IL 60208 USA (e-mail: daniel.ludvig@northwestern.edu).

Levi Hargrove is with the Shirley Ryan AbilityLab, Center for Robotics and Biosystems, and Department of Physical Medicine and Rehabilitation, Northwestern University, Chicago, IL 60208 USA (e-mail: l-hargrove@northwestern.edu).

Eric J. Perreault is with the Department of Physical Medicine and Rehabilitation, Department of Biomedical Engineering, Shirley Ryan AbilityLab and Center for Robotics and Biosystems, Chicago, IL 60208 USA (e-mail: e-perreault@northwestern.edu).

Kevin M. Lynch is with the Center for Robotics and Biosystems and Department of Mechanical Engineering, Northwestern University, Chicago, IL 60208 USA (e-mail: kmlynch@northwestern.edu).

José L. Pons is with the Shirley Ryan AbilityLab, Center for Robotics and Biosystems, Department of Mechanical Engineering, Department of Biomedical Engineering, and Department of Physical Medicine and Rehabilitation, Northwestern University, Chicago, IL 60208 USA (e-mail: jpons@sralab.org).

This article has supplementary downloadable material available at <https://doi.org/10.1109/TRO.2024.3359541>, provided by the authors.

Digital Object Identifier 10.1109/TRO.2024.3359541

simplified the dynamic model by treating the legs as independent double pendulums, or they did not close the loop with interaction force feedback. The proposed whole-exoskeleton closed-loop compensation (WECC) method calculates the interaction torques during the complete gait cycle by using whole-body dynamics and joint torque measurements on a hip-knee exoskeleton. Furthermore, it uses a constrained optimization scheme to track desired interaction torques in a closed loop while considering physical and safety constraints. We evaluated the haptic transparency and dynamic interaction torque tracking of WECC control on three subjects. We also compared the performance of WECC with a controller based on a simplified dynamic model and a passive version of the exoskeleton. The WECC controller results in a consistently low absolute interaction torque error during the whole gait cycle for both zero and nonzero desired interaction torques. In contrast, the simplified controller yields poor performance in tracking desired interaction torques during the stance phase.

**Index Terms**—Assistive robots, exoskeletons, interaction force control, physical human–robot interaction, rehabilitation robots.

## I. INTRODUCTION

LOWER limb exoskeletons are used to assist impaired individuals in their daily life and as a tool for physical rehabilitation in clinical settings [1], [2]. They are also increasingly used to augment the abilities of healthy individuals [3]. In each of these applications, the exoskeleton must be capable of regulating the interaction forces and torques between the user and the exoskeleton, both for the safety of the user and the effectiveness of the control mode.

As an example, the *transparent* control mode attempts to zero the interaction forces between the user and the exoskeleton. Transparency is useful for comparison when evaluating new rehabilitation control strategies [4] and for allowing users to move freely when wearing assistive devices [5]. Other control modes, used in rehabilitation, include “assist as needed” (AAN) and resistive control for robot-aided gait therapy [6]. With AAN, the robot provides only as much assistance force as needed to complete a given task [7]. In resistive and error-augmentation methods, force is applied to make the task more challenging, which accelerates relearning of motor tasks [4], [8].

An important part of controlling interaction forces is compensating the weight of the lower limb exoskeleton. How the weight of the exoskeleton is transferred to the ground or the user depends on its design. There are three main categories of design.

- 1) *Grounded Trunk:* The trunk of the exoskeleton is fixed relative to a treadmill structure [9], [10], [11]. Due to the grounded trunk, only the masses of the individual leg links are felt by the user, and these masses can be compensated with active control.
- 2) *Floating-Base (trunk) Without Feet:* These exoskeletons are designed for unrestricted overground walking and do not contact the ground [12], [13], [14]. Partial gravity compensation can be achieved for the swing leg, but it is not possible for the exoskeleton to completely carry its own weight since there is no contact with the ground. Such exoskeletons are designed to be as light as possible, which limits their maximum assistance/resistance and battery life.
- 3) *Floating-Base With Feet:* These exoskeletons are designed for unrestricted overground walking and have feet that contact the ground [15], [16], [17], [18], [19], [20], [21]. The weight of the exoskeleton can be transferred to the ground through the exoskeleton's foot contact. While this allows for stronger actuators and larger batteries, it comes at the cost of more complicated controllers for accurate interaction force control.

In this article, we focus on floating-base lower limb exoskeletons with feet, for which controlling interaction forces remains an open problem [17], [22]. Accurate interaction force control will enable natural implementations of AAN, resistive, and error-augmentation methods in overground walking therapy using rehabilitation exoskeletons. Floating-base exoskeletons with feet also allow the possibility of larger assistive forces and longer battery life.

Due to the high torque requirements of floating-base exoskeletons with feet, high reduction ratios are used, which results in high friction and apparent inertia of motor rotors [23]. Also, these exoskeletons are heavy due to powerful actuators and large batteries. Therefore, it is essential to compensate for these factors to accurately control the interaction forces and torques between the user and the exoskeleton.

Another challenge is measuring the interaction torques between the human and the exoskeleton. Grounded exoskeletons typically have a small number of contacts with the user, and interaction forces can be directly measured by force sensors implemented at the contacts [10], [24], [25]. In contrast, floating-base exoskeletons have broadly distributed contacts with the user, including at the trunk and foot. This makes it challenging to implement force/torque sensors at all contacts. Therefore, it is required to indirectly estimate the interaction forces and torques through other sensory information.

In this article, we present a novel method to estimate and control user-exoskeleton interaction torques during the complete gait cycle of a floating-base hip-knee exoskeleton with feet. The controller, which is based on constrained optimization, outperforms the state of the art in achieving transparency (zero impedance) and nonzero impedances in the user-exoskeleton interaction behavior.

The context of the contribution of this article is established by the related work below.

### A. Related Work

Previous studies on controlling interaction forces with floating-base lower limb exoskeletons with feet can be divided into three main categories.

1) *Whole-Body Dynamics Compensation With No Interaction Force Feedback:* A lower limb exoskeleton can be modeled as a floating-base system considering all links and joints together, similar to a bipedal robot [26], [27]. Vantilt et al. [16] implemented a whole-body floating-base model while considering external contact constraints, such as ground contact or contact with a stool. They estimated the contact forces based on a complementary energy method [28]. However, this method does not allow the calculation of interaction torques at the nonstatic contact points between the human and exoskeleton. Camardella et al. [15] also modeled the full-body dynamics based on the user-dependent continuous interpolation between left and right stance dynamics. These studies compensated for the gravitational and Coriolis torques calculated using the whole-body model. However, modeling errors were not corrected with interaction force feedback, and desired interaction torques were used only as a feedforward term.

2) *Simplified Double Pendulum Model With Interaction Force Feedback:* Andrade et al. [17], [18], and Tu et al. [19] employed a simpler, nonwhole-body model of the exoskeleton to help estimate interaction torques. In this simplified model, each leg is modeled as an independent double pendulum 2R robot. When the leg is in swing and stance, the hip and ankle joints are assumed to be pinned, respectively. This model is used to calculate the feedforward compensation torques, which are subtracted from the joint torque measurements to estimate the interaction torques between the human and exoskeleton. Interaction torque estimation is used as the input of a proportional–derivative (PD) or admittance controller.

Since the backpack is not modeled and the legs are modeled independently, the dynamic compensation torques and interaction torque estimates are not accurate for the stance leg. With this approach, the stance leg carries only its own weight instead of the weight of the entire exoskeleton. While this might be acceptable for light or grounded exoskeletons, it is not accurate for exoskeletons designed for overground walking that provide a high level of support and long battery life.

3) *User-Dependent or User-Instrumented Approaches:* Since physical parameters and walking gaits vary from user to user, some interaction force controllers require additional sensors to be affixed to the user and/or custom tuned for each user.

Sharifi et al. [20] implemented a neural network scheme to learn the whole-body dynamics of the exoskeleton together with the user. While this method does not require additional sensors to measure the joint torques, the main drawback is user-dependent learned dynamics, and a training phase is required for each user. Kazerooni et al. [21] implemented a hybrid controller where the exoskeleton's stance leg follows the joint positions of the user to provide haptic transparency. The joint positions of the user's leg are measured by inclinometers attached to it. Moreover, the proposed method is for haptic transparency only; if the desired

TABLE I  
SELECTED FEATURES OF THE INTERACTION FORCE/TORQUE CONTROL STUDIES

Reference	Model	Interaction force feedback	User dependent	Instrumentation on user	Physical/safety limit implementation
Camardella et al., 2021 [15]	Whole-body	No	Yes	No	No
Vantilt et al., 2019 [16]	Whole-body	No	No	No	No
Andrade et al., 2019–21[17], [18]	Independent double pendulums	PD controller	No	No	No
Tu et al., 2020 [19]	Independent double pendulums	Admittance controller	No	No	No
Sharifi et al., 2021 [20]	Whole-body (learnt by NN)	No	Yes	No	No
Kazerooni et al., 2006 [21]	3-link for swing no model for stance (position control)	Sensitivity Amplification	No (transparency) Yes (non-zero reference)	Yes	No
Our proposed method (WECC)	Whole-body	Admittance controller	No	No	Yes

Note that this article focuses on floating-base lower limb exoskeletons with feet. Therefore, this table does not include studies with grounded exoskeletons and floating-base lower limb exoskeletons without feet.

interaction force is nonzero, a model of the user-dependent interaction properties are needed.

4) *Summary:* Selected features of interaction force/torque control studies on floating-base lower limb exoskeletons that contact the ground are presented in Table I. These studies can be categorized into three main groups. First, there are studies where the whole-body dynamics of the exoskeleton are compensated with no interaction force feedback [15], [16], [20]. Second, some studies modeled the exoskeleton as two independent legs with no consideration of the backpack [17], [18], [19]. These studies implemented PD or admittance controllers based on the interaction force/torque error. Third, there are methods that require additional instrumentation on the user [21] or user-dependent learning for model or gait state estimation [15], [20]. None of these proposed control strategies implement optimization methods to enforce physical or safety limits to avoid actuator saturation or to constrain the motion to satisfy safety conditions. To the best of the authors' knowledge, there is no study that calculates interaction forces with full-body dynamics during the whole gait cycle and uses this estimation in a closed-loop control for a floating-base lower limb exoskeleton that is in contact with the ground.

### B. Contributions

In this article, we propose a novel subject-independent method to calculate interaction forces during both single and double stance configurations based on a whole-body dynamic model. Moreover, we propose constrained optimization combined with a virtual model controller to achieve desired interaction torques while considering physical and safety constraints. We call the proposed method *whole-exoskeleton closed-loop compensation* (WECC) because whole-body dynamics of the exoskeleton is compensated and considered in the closed-loop controller.

We evaluated the transparency and spring-damper haptic-rendering performance of our proposed WECC controller on treadmill walking. We compared the performance of the WECC controller to a control approach based on a simplified dynamic model of the exoskeleton (the "simplified" condition), where the legs are modeled as double pendulums independent of one another and the backpack is ignored [17], [18], [19], [23]. For

transparency evaluations, we also tested the performance of a passive version of the exoskeleton with disassembled drives (the "no-drive" condition). We observed that the transparency of the swing leg was similar under the three conditions (WECC, simplified, and no-drive), but our proposed WECC method outperformed the simplified controller and the no-drive condition for the stance leg. In nonzero impedance haptic rendering, the WECC and simplified controllers performed similarly for the swing leg, but our WECC controller tracked the desired interaction torques better for the stance leg.

The core contributions of this article are as follows.

- 1) A continuous whole-body forward dynamical model for the whole gait cycle is developed based on the ratios of the vertical ground reaction forces (GRF) at the feet.
- 2) A novel method to estimate the interaction forces during both single and double stance configurations is proposed.
- 3) A constrained-optimization-based virtual mass controller is implemented that considers the underactuation of the exoskeleton and its physical/safety constraints to control the interaction torques.
- 4) The transparency and haptic rendering performance of our proposed WECC controller is compared with a state-of-the-art controller based on a simplified dynamic model.

## II. SYSTEM DESCRIPTION AND MODELING

### A. Lower Limb Exoskeleton: *ExoMotus-X2*

A four-degrees-of-freedom (DOF) lower limb exoskeleton (*ExoMotus-X2*, Fourier Intelligence, Singapore), shown in Fig. 1, was adapted and used as a platform to test the proposed interaction torque controller. This exoskeleton has four total active DOF at the hip and knee joints, and passively allows motion at the ankle joints. Each active joint is driven by a Maxon EC60 100 W motor with a 1:122.5 reduction ratio obtained via harmonic gearing and a belt. Copley Accelnet ACK-055-06 motor drivers are used to control the motors. A peak torque of 80 Nm and a peak velocity of 3.2 rad/s can be obtained at each joint.

Due to the high friction caused by the large reduction ratio, it is not feasible to estimate the joint torques by only measuring



Fig. 1. ExoMotus-X2 lower limb exoskeleton, featuring a close-up view of the strain gauge implementation (left) and a user wearing the exoskeleton (right).

the current through the motors. Therefore, we modified the ExoMotus-X2 exoskeleton to add joint torque sensors at each driven joint. Each torque sensor consists of a full Wheatstone bridge with four strain gauges on the limb just distal to the joint, similar to the method presented by Claros et al. [29]. These custom joint torque sensors provide measurements with a resolution of 0.3 Nm and 0.1 Nm at the hip and knee joints, respectively. The strain gauges were calibrated by immobilizing the joints and hanging known weights at known locations whereas the exoskeleton was suspended by backpack attachment points. A close-up view of the strain gauge is shown in Fig. 1.

An inertial measurement unit (IMU) (Tech-IMU V4 by Technaid S.L.) is mounted on the backpack to measure the orientation and angular velocity of that link. Using the encoder measurements from each motor and orientation estimation of the backpack, the orientation of each link in the sagittal plane with respect to the gravity vector is estimated. In addition, eight 3-DOF force plates (9047B, Kistler) under a custom instrumented split-belt treadmill are used to measure GRF at each foot.<sup>1</sup> Furthermore, to have a tighter connection with the upper body, an additional trunk brace was adopted from another lower limb exoskeleton (Exo-H3, Technaid S.L.).

Communication with motors and onboard sensors is established over a controller area network (CAN) bus using the

<sup>1</sup>The external footplates provide ground truth, but the controller uses only relative GRF rather than absolute GRF, and estimates of these relative forces may be provided by sensors on the exoskeleton itself. This is discussed further in Sections III and VI.

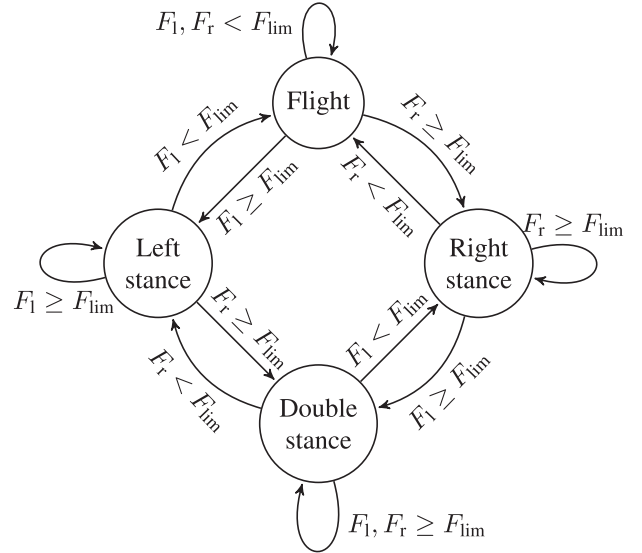


Fig. 2. State machine structure of the gait states. The variables  $F_l$  and  $F_r$  are the left foot and right foot vertical force readings, respectively. The threshold force that triggers state change is represented by  $F_{lim}$ . This threshold can be an absolute force value or a ratio of the total vertical forces. When this state machine is used in real-time control, states are not allowed to change more than once every 150 ms for robustness to noise. During walking, the focus of this article, the flight state never occurs.

CANOpen communication protocol. To minimize communication delay and allow real-time visualization and tuning capabilities, an external PC is connected to the exoskeleton by a tether. Analog force plate readings are acquired with an Arduino Mega board connected to the same PC. The controllers and applications are implemented on an open-source software stack called CANOpen robot controller (CORC) [30] based on ROS and C++. High-level controller commands and sensor measurements are updated at 333 Hz, whereas the low-level current controller of the motors runs at 15 kHz.

### B. Dynamic Model

Our proposed WECC control method is based on a whole-body model where we incorporate the sagittal plane dynamics of every link of the exoskeleton, including the backpack.

1) *Whole-Body Dynamics:* The exoskeleton is modeled as a floating-base five-link mechanism with four active joints. The dynamics of the human user are not modeled but are incorporated into the exoskeleton dynamics as a source of external torque at each joint. For each gait state, the constraints on the system and the equations of motion are modified accordingly. These gait states are no ground contact (*flight*), contact by a single foot (*single stance*), and contact by two feet (*double stance*). Fig. 2 presents the gait state machine.

a) *Single Stance:* In single stance, the ankle of the stance leg is assumed to be hinged to the ground. With this assumption, the exoskeleton has five DOF. The generalized coordinates and equations of motion are

$$\mathbf{M}_i(\mathbf{q})\ddot{\mathbf{q}} + \mathbf{b}_i(\mathbf{q}, \dot{\mathbf{q}}) + \mathbf{g}_i(\mathbf{q}) = \mathbf{S}^\top \boldsymbol{\tau}_{\text{joint}} + \boldsymbol{\tau}_{\text{int}}, \quad i \in \{\text{ls, rs}\} \quad (1)$$

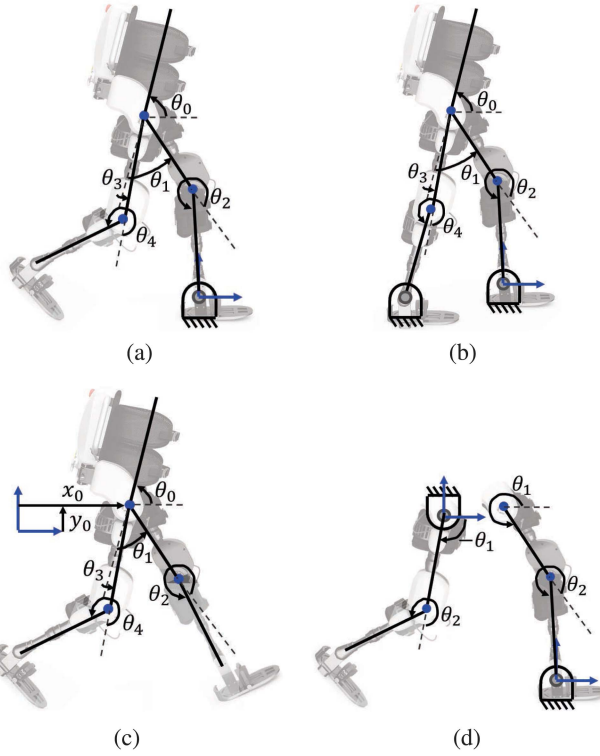


Fig. 3. Different gait states and representation of the generalized coordinates. Whole-body model representations are shown in subfigures (a), (b), and (c). Subfigure (d) corresponds to the stance and swing phases of the simplified model. (a) Single stance. (b) Double stance. (c) Flight. (d) Simplified.

where  $\mathbf{q} = [\theta_0, \theta_1, \theta_2, \theta_3, \theta_4]^\top$  are the generalized coordinates corresponding to the backpack, hip, and knee angles, as shown in Fig. 3(a). The matrix and vectors  $\mathbf{M}_i \in \mathbb{R}^{5 \times 5}$ ,  $\mathbf{b}_i \in \mathbb{R}^5$ , and  $\mathbf{g}_i \in \mathbb{R}^5$ , are the mass matrix, Coriolis and centrifugal torques, and gravitational torques, respectively, during left stance ( $i = \text{ls}$ ) and right stance ( $i = \text{rs}$ ). The vector  $\boldsymbol{\tau}_{\text{joint}} \in \mathbb{R}^4$  corresponds to joint torques, and  $\mathbf{S} = [0_{4 \times 1}, \mathbb{I}_{4 \times 4}]$  is a selection matrix of actuated joints. The interaction torques applied to the exoskeleton by the user are given by the vector  $\boldsymbol{\tau}_{\text{int}} \in \mathbb{R}^5$ .

*b) Double Stance:* This state can be expressed as an extension of the single stance model where one ankle is assumed to be hinged on the ground and external forces are applied on the other ankle

$$\mathbf{M}_i(\mathbf{q})\ddot{\mathbf{q}} + \mathbf{b}_i(\mathbf{q}, \dot{\mathbf{q}}) + \mathbf{g}_i(\mathbf{q}) = \mathbf{S}^\top \boldsymbol{\tau}_{\text{joint}} + \boldsymbol{\tau}_{\text{int}} + \mathbf{J}_j^\top \boldsymbol{\Gamma}_j, \quad (2)$$

$$(i, j) \in \{(\text{ls}, \text{l}), (\text{rs}, \text{l})\}$$

where  $\mathbf{J}_j$  and  $\boldsymbol{\Gamma}_j$  correspond to the contact Jacobian of the left ( $j = \text{l}$ ) or right ( $j = \text{r}$ ) ankle and the external forces at that point, respectively. Multiplying (2) by the transpose of the constraint matrix  $\mathbf{H} \in \mathbb{R}^{5 \times 3}$ , where  $\mathbf{JH} = 0$ , results in the following equation of motion:

$$\mathbf{H}^\top (\mathbf{M}_i(\mathbf{q})\ddot{\mathbf{q}} + \mathbf{b}_i(\mathbf{q}, \dot{\mathbf{q}}) + \mathbf{g}_i(\mathbf{q}) - \boldsymbol{\tau}_{\text{int}}) = \mathbf{H}^\top \mathbf{S}^\top \boldsymbol{\tau}_{\text{joint}}, \quad (3)$$

$$i \in \{\text{ls}, \text{rs}\}.$$

The two position constraints on the other ankle represented in the constraint matrix  $\mathbf{H}$  map the 5-D (2) onto the 3-D controllable

space. Any three of the five coordinates may be chosen as the generalized coordinates.<sup>2</sup> Since there are only three DOF, the system is overactuated during double stance; there exists a 1-D null space of internal “cocontraction” torques that have no impact on motion. Overactuation in double stance complicates the estimation of interaction torques, as discussed in Section III, and may cause a discontinuity in the equations of motion and the dynamic compensation torques during transitions between single and double stance.

To sidestep these issues, we approximate double stance as a transition from left stance to right stance or vice versa

$$\mathbf{M}_{\text{ds}}(\mathbf{q})\ddot{\mathbf{q}} + \mathbf{b}_{\text{ds}}(\mathbf{q}, \dot{\mathbf{q}}) + \mathbf{g}_{\text{ds}}(\mathbf{q}) = \mathbf{S}^\top \boldsymbol{\tau}_{\text{joint}} + \boldsymbol{\tau}_{\text{int}} \quad (4)$$

where

$$\mathbf{M}_{\text{ds}} = \alpha \mathbf{M}_{\text{ls}} + (1 - \alpha) \mathbf{M}_{\text{rs}} \quad (5)$$

$$\mathbf{b}_{\text{ds}} = \alpha \mathbf{b}_{\text{ls}} + (1 - \alpha) \mathbf{b}_{\text{rs}} \quad (6)$$

$$\mathbf{g}_{\text{ds}} = \alpha \mathbf{g}_{\text{ls}} + (1 - \alpha) \mathbf{g}_{\text{rs}}. \quad (7)$$

The variable  $\alpha$  in (5)–(7) corresponds to the interpolation factor from left-stance dynamics to right-stance dynamics. These interpolated dynamics are particular solutions to the equations of motion (3), as proven in Appendix D. The interpolation factor  $\alpha$  is calculated based on the ratio of the left vertical ground reaction force to the sum of both vertical GRF

$$\alpha = \frac{F_{\text{l},y}}{F_{\text{l},y} + F_{\text{r},y}} \quad (8)$$

where  $F_{\text{l},y}$  and  $F_{\text{r},y}$  are left and right vertical GRF, respectively. The rationale for defining the  $\alpha$  based on the ratios of the vertical GRF is presented in Appendix D. Interpolating the equation of motion from left-stance dynamics to right-stance dynamics allows smooth continuous modeling of the whole gait cycle that is consistent with the weight transition of the exoskeleton during walking. The difference of this method from the work of Camardella et al. [15] is that their kinematic-based gait segmentation is user-dependent and requires a training procedure.

*c) Flight:* In the flight state, the only external forces on the exoskeleton are due to interaction with the user. While this state does not occur during walking, we use this state’s equation of motion for exoskeleton parameter estimation, as described in Section II-C. The equation of motion in generalized coordinates is

$$\mathbf{M}_{\text{fly}}(\mathbf{q}_{\text{fly}})\ddot{\mathbf{q}}_{\text{fly}} + \mathbf{b}_{\text{fly}}(\mathbf{q}_{\text{fly}}, \dot{\mathbf{q}}_{\text{fly}}) + \mathbf{g}_{\text{fly}}(\mathbf{q}_{\text{fly}}) = \mathbf{S}_{\text{fly}}^\top \boldsymbol{\tau}_{\text{joint}} + \boldsymbol{\tau}_{\text{int}}^{\text{fly}} \quad (9)$$

where  $\mathbf{q}_{\text{fly}} = [x_0, y_0, \theta_0, \theta_1, \theta_2, \theta_3, \theta_4]$  is a vector of generalized coordinates corresponding to the linear and angular positions of the backpack and the hip and knee joint angles, as shown in Fig. 3(c). The variable  $\mathbf{M}_{\text{fly}} \in \mathbb{R}^{7 \times 7}$  is the mass matrix,  $\mathbf{b}_{\text{fly}} \in \mathbb{R}^7$  is a vector of Coriolis and centrifugal forces, and  $\mathbf{g}_{\text{fly}} \in \mathbb{R}^7$  a vector of gravitational forces. The variable  $\mathbf{S}_{\text{fly}} = [0_{4 \times 3}, \mathbb{I}_{4 \times 4}]$  is a selection matrix of actuated joints, and  $\boldsymbol{\tau}_{\text{int}}^{\text{fly}} \in \mathbb{R}^7$  is a vector of interaction forces and torques applied to the exoskeleton by the user.

<sup>2</sup> Interested readers may refer to [31] for the details of the constraint matrix  $\mathbf{H}$  and (2) and (3).

TABLE II

ESTIMATED MASSES AND INERTIAS (ABOUT AXES THROUGH THE COM AND PERPENDICULAR TO THE SAGITTAL PLANE) OF LINKS AND MOTOR ROTORS OF THE EXOMOTUS-X2 EXOSKELETON

Link	$m$ [kg]	$L$ [ $\text{kgm}^2$ ]
Backpack	10.3	0.201
Upper thigh	0.7	0.002197
Lower thigh	2.14	0.005901
Upper shank	0.64	0.002346
Lower shank	0.47	0.0007941
Foot	1.25	0.004441
Rotor (apparent)	-	$1.24610^{-4} \times 122.5^2 = 1.87$

2) *Simplified Dynamics:* The dynamics described above are used in our proposed WECC controller. A simpler model, described here, considers each leg of the exoskeleton as an independent double pendulum and excludes the backpack [14], [19], [23], [24], [25], [32]. We use this model for comparison to our approach. The hip joint is considered grounded for a swing leg, and the ankle joint is considered fixed to the ground for a stance leg, as shown in Fig. 3(d).

The equation of motion can be written

$$\mathbf{M}_i(\mathbf{q})\ddot{\mathbf{q}} + \mathbf{b}_i(\mathbf{q}, \dot{\mathbf{q}}) + \mathbf{g}_i(\mathbf{q}) = \boldsymbol{\tau}_{\text{joint}} + \boldsymbol{\tau}_{\text{int}}, \quad i \in \{\text{st, sw}\} \quad (10)$$

where  $\mathbf{q} = [\theta_1, \theta_2]^\top$  are the hip and knee joint positions, respectively. The variables  $\mathbf{M}_i \in \mathbb{R}^{2 \times 2}$ ,  $\mathbf{b}_i \in \mathbb{R}^2$ , and  $\mathbf{g}_i \in \mathbb{R}^2$  are the mass matrix, Coriolis and centrifugal torques, and gravitational torques, respectively, during stance ( $i = \text{st}$ ) and swing ( $i = \text{sw}$ ) of a single leg.

### C. Parameter Estimation

Inertial parameters such as mass, mass moment of inertia, and center of mass (CoM) locations of each link were estimated from the computer aided drawing (CAD) model of the ExoMotus-X2 exoskeleton. Dynamic terms such as  $\mathbf{M}$ ,  $\mathbf{b}$ , and  $\mathbf{g}$  are defined as a function of these parameters, adjustable link lengths, and instantaneous joint states. Their values are calculated at every time instant. Some of these parameters are presented in Table II. Note that the largest inertias come from the apparent rotor inertia, which is proportional to the square of the reduction ratio ( $\text{RR} = 122.5$ ).

The high gear ratios also result in significant friction at each joint. Friction at the joints is modeled as viscous friction combined with Coulomb friction as a function of joint speed

$$\boldsymbol{\tau}_{\text{friction}} = \mathbf{c}_0 \odot \text{sign } \dot{\boldsymbol{\theta}} + \mathbf{c}_1 \odot \dot{\boldsymbol{\theta}} \quad (11)$$

where  $\dot{\boldsymbol{\theta}}$  is the vector of joint velocities and  $\mathbf{c}_0$  and  $\mathbf{c}_1$  are the vectors of Coulomb and viscous coefficients, respectively. The symbol  $\odot$  indicates elementwise Hadamard product.

To conduct the parameter estimation experiments, the exoskeleton was suspended by backpack attachment points. Chirp motor torque commands with increasing frequency up to 3 Hz at different amplitudes were simultaneously given to the hip and knee joints of a single leg

$$\boldsymbol{\tau}_{\text{motor}} = A_i \sin(6\pi t^2/T) \quad (12)$$

TABLE III  
ESTIMATED FRICTION PARAMETERS OF THE EXOMOTUS-X2 EXOSKELETON  
AND  $R^2$  OF THE FIT

Joint	$c_0$ [Nm]	$c_1$ [Nms]	$R^2$
Left hip	5.01	4.58	0.96
Right hip	3.26	4.67	0.94
Left knee	4.30	3.25	0.96
Right knee	4.45	5.16	0.96

where  $A_i \in \{7.5, 10, 12.5, 15\}$  Nm and  $T = 60$  s for each amplitude. Joint positions were measured during the experiments.

The joint torques,  $\boldsymbol{\tau}_{\text{joint}}$ , in (1), (2), and (9) are the sum of motor torques,  $\boldsymbol{\tau}_{\text{motor}}$ , and friction compensation torques,  $\boldsymbol{\tau}_{\text{friction}}$

$$\boldsymbol{\tau}_{\text{joint}} = \boldsymbol{\tau}_{\text{motor}} + \boldsymbol{\tau}_{\text{friction}}. \quad (13)$$

As there was no contact with the ground at this configuration, the equation of motion of the flight state was used to estimate the frictional parameters. Equation (9) is rewritten to include viscous and Coulomb friction constants by substituting  $\boldsymbol{\tau}_{\text{joint}}$  in (13) into (9)

$$\begin{aligned} & \mathbf{M}_{\text{fly}}(\mathbf{q}_{\text{fly}})\ddot{\mathbf{q}}_{\text{fly}} + \mathbf{b}_{\text{fly}}(\mathbf{q}_{\text{fly}}, \dot{\mathbf{q}}_{\text{fly}}) + \mathbf{g}_{\text{fly}}(\mathbf{q}_{\text{fly}}) \\ &= \mathbf{S}_{\text{fly}}^\top(\boldsymbol{\tau}_{\text{motor}} + \mathbf{c}_0 \odot \text{sign } \dot{\boldsymbol{\theta}} + \mathbf{c}_1 \odot \dot{\boldsymbol{\theta}}) + \boldsymbol{\tau}_{\text{int}}. \end{aligned} \quad (14)$$

Recorded backpack and joint angular positions, joint angular velocities, joint angular accelerations, and CAD-based inertial parameters were used to calculate  $\mathbf{M}_{\text{fly}}$ ,  $\mathbf{b}_{\text{fly}}$ , and  $\mathbf{g}_{\text{fly}}$  at each time instant. Joint accelerations were calculated by taking the derivative of the joint velocities numerically by the nine-point difference method [33]. Then, in MATLAB, accelerations were low-pass filtered with a cutoff frequency of 10 Hz, while also incorporating delay compensation. Since the exoskeleton was hung from the backpack at a fixed location,  $\ddot{x}$  and  $\ddot{y}$  were negligible. Also, as there was no user in the exoskeleton, rotational components of  $\boldsymbol{\tau}_{\text{int}}$  were zero. The coefficients  $\mathbf{c}_0$  and  $\mathbf{c}_1$  were solved using the recorded data by least-square minimization on (14). Estimated friction parameters for each joint and the  $R^2$  value of the fit are presented in Table III.

## III. INTERACTION TORQUE CONTROLLER

### A. Interaction Torque Estimation

Estimating the interaction torques between the human and exoskeleton plays a significant role in the transparency and haptic rendering capabilities of the robot. Placing force/torque sensors at every contact point between the human and exoskeleton would theoretically be ideal for measuring the interaction. However, due to the distributed contacts between the human and the exoskeleton and practical challenges of this approach, we chose to estimate the interaction torques through joint torque measurements. Joint torques were measured using our custom joint-torque sensors mentioned in Section II-A.

Because the ExoMotus-X2 exoskeleton was designed for individuals with sensorimotor impairments and, therefore, limited walking ability, we estimated the interaction torque during single and double stance only, excluding the flight state.

1) *Single Stance Interaction Torque Estimation:* We estimate the interaction torque during single stance by subtracting the

gravitational and Coriolis forces from the joint torque readings

$$\boldsymbol{\tau}_{\text{int}} = -\boldsymbol{S}^T \boldsymbol{\tau}_{\text{joint}} + \boldsymbol{b}_i(\boldsymbol{q}, \dot{\boldsymbol{q}}) + \boldsymbol{g}_i(\boldsymbol{q}), \quad i \in \{\text{ls}, \text{rs}\}. \quad (15)$$

As shown in Table II, the largest contributors to the inertial terms are the apparent rotor inertias due to the high reduction ratios. However, since the strain gauges are placed at the link (i.e., after the motor), the torque measurements are not affected by the apparent rotor inertia. In addition, because the links have relatively low inertia and the walking speed during the experiment is not high, the effects of inertial forces are significantly smaller compared with gravitational forces. Therefore, acceleration-dependent inertial components are neglected in the interaction torque estimation.

It is worth noting that  $\boldsymbol{\tau}_{\text{int}} \in \mathbb{R}^5$ , which includes the interaction torque at the backpack joint in addition to the four leg joints.

2) *Double Stance Interaction Torque Estimation*: Interaction torque estimation can be expressed by extending the left and right stance model with the additional external contact force at the right and left foot, respectively,

$$\boldsymbol{\tau}_{\text{int}} = -\boldsymbol{S}^T \boldsymbol{\tau}_{\text{joint}} + \boldsymbol{b}_{\text{ls}}(\boldsymbol{q}, \dot{\boldsymbol{q}}) + \boldsymbol{g}_{\text{ls}}(\boldsymbol{q}) - \boldsymbol{J}_{\text{r}}^T \boldsymbol{F}_{\text{r}} \quad (16)$$

$$\boldsymbol{\tau}_{\text{int}} = -\boldsymbol{S}^T \boldsymbol{\tau}_{\text{joint}} + \boldsymbol{b}_{\text{rs}}(\boldsymbol{q}, \dot{\boldsymbol{q}}) + \boldsymbol{g}_{\text{rs}}(\boldsymbol{q}) - \boldsymbol{J}_{\text{l}}^T \boldsymbol{F}_{\text{l}} \quad (17)$$

where  $\boldsymbol{J}_i$  is the ankle Jacobian and  $\boldsymbol{F}_i$  is the external force applied on the left ( $i = \text{l}$ ) and right ( $i = \text{r}$ ) foot. Combining (16) and (17) results in ten equations with rank seven. Nine unknowns in these equations are the 5-D interaction torque vector  $\boldsymbol{\tau}_{\text{int}}$ , and the 2-D contact forces at the left ( $\boldsymbol{F}_{\text{l}}$ ) and right ( $\boldsymbol{F}_{\text{r}}$ ) feet. Since there are seven independent equations and nine unknowns, it is not possible to uniquely solve for the interaction torque vector without additional information.

Ratios of the vertical GRF and the direction of the GRF in the sagittal plane are used to resolve the redundancy. In this study, we used external force plates to measure these terms, but they can also be obtained by wearable sensors, or sensors instrumented onto the exoskeleton, as explained in Section VI-C.

The vertical GRF ratio  $\alpha$  is introduced in (8) and is also used for the equations of motion during double stance. The direction of the force can be expressed as the ratio of the horizontal and vertical forces

$$\gamma = \frac{F_{\text{l},x}}{F_{\text{l},y}}. \quad (18)$$

Equations (8) and (16)–(18) are converted to a system of linear equations as  $\mathbf{K}\boldsymbol{\xi} = \mathbf{m}$ , where

$$\begin{aligned} \mathbf{K} &= \begin{bmatrix} \boldsymbol{J}_{\text{r}}^T & 0_{5 \times 2} & \mathbb{I}_{5 \times 5} \\ 0_{5 \times 2} & \boldsymbol{J}_{\text{l}}^T & \mathbb{I}_{5 \times 5} \\ [0, 1] & [0, -\alpha/(1-\alpha)] & 0_{1 \times 5} \\ [0, 0] & [1, -\gamma] & 0_{1 \times 5} \end{bmatrix} \\ \boldsymbol{\xi} &= [F_{\text{r},x} \ F_{\text{r},y} \ F_{\text{l},x} \ F_{\text{l},y} \ \boldsymbol{\tau}_{\text{int}}^T]^T \\ \mathbf{m} &= \begin{bmatrix} -\boldsymbol{S}^T \boldsymbol{\tau}_{\text{joint}} + \boldsymbol{b}_{\text{ls}}(\boldsymbol{q}, \dot{\boldsymbol{q}}) + \boldsymbol{g}_{\text{ls}}(\boldsymbol{q}) \\ -\boldsymbol{S}^T \boldsymbol{\tau}_{\text{joint}} + \boldsymbol{b}_{\text{rs}}(\boldsymbol{q}, \dot{\boldsymbol{q}}) + \boldsymbol{g}_{\text{rs}}(\boldsymbol{q}) \\ 0 \\ 0 \end{bmatrix} \end{aligned} \quad (19)$$

TABLE IV  
VIRTUAL MASS VALUES FOR EACH LINK USED DURING THE EXPERIMENTATION

Link	Gait State	Virtual Mass [kgm <sup>2</sup> ]
Backpack	Single Stance	2
Backpack	Double Stance	3.5
Thigh	Single Stance	0.7
Thigh	Double Stance	1.2
Shank	Single Stance	0.5
Shank	Double Stance	0.87

and solved for the interaction torques.

3) *Simplified Interaction Torque Estimation*: With the simplified double pendulum model, interaction torques at the hip and knee joints can be estimated by subtracting the dynamic effects from the joint torque measurements

$$\boldsymbol{\tau}_{\text{int}} = \boldsymbol{\tau}_{\text{joint}} + \boldsymbol{b}_i(\boldsymbol{q}, \dot{\boldsymbol{q}}) + \boldsymbol{g}_i(\boldsymbol{q}), \quad i \in \{\text{st}, \text{sw}\}. \quad (20)$$

It is important to note that with the simplified method,  $\boldsymbol{\tau}_{\text{int}} \in \mathbb{R}^2$  does not include the interaction torque at the backpack. Moreover, because the backpack link is not incorporated into the dynamic model, the backpack's weight is not subtracted, resulting in inaccurate interaction torque estimation for exoskeletons with heavy backpacks.

## B. Control

1) *Virtual Mass Controller*: To control the interaction torques between the human and the exoskeleton, we implemented a *virtual mass controller* [34], [35] to simulate a desired mass or inertia, with no damping, of each generalized coordinate of the exoskeleton. This can be achieved by setting the desired generalized acceleration to

$$\ddot{\boldsymbol{q}}^* = \mathbf{M}_{\text{virt}}^{-1} (\boldsymbol{\tau}_{\text{int}} - \boldsymbol{\tau}_{\text{int}}^*) \quad (21)$$

where  $\boldsymbol{\tau}_{\text{int}}^*$  is the desired interaction torque, e.g., zero for transparency or nonzero for other desired impedances.

Under the assumptions of perfect control of the generalized accelerations and accurate interaction torque estimation with little delay, this equation shows that the interaction torque error is proportional to the chosen virtual mass matrix  $\mathbf{M}_{\text{virt}}$  and joint accelerations. Therefore, lowering  $\mathbf{M}_{\text{virt}}$  results in better interaction torque tracking. Obviously,  $\mathbf{M}_{\text{virt}}$  cannot be decreased below a certain limit due to the actuation limits, modeling errors, and communication delays. Moreover, the limit on the virtual mass also depends on the interaction properties between the human and exoskeleton. While the damping due to the soft tissues of the user makes the system more stable, a very stiff connection would increase the minimum allowable virtual mass for a stable response.

We used a diagonal  $\mathbf{M}_{\text{virt}}$  and tuned the virtual mass parameter for each generalized coordinate independently. The tuning process was done on a pilot user (a nonparticipant) by reducing each virtual mass as much as possible before compromising the stability of the control. The parameters were then verified with two other pilot users. This process resulted in different virtual mass parameters for single stance and double stance, as shown

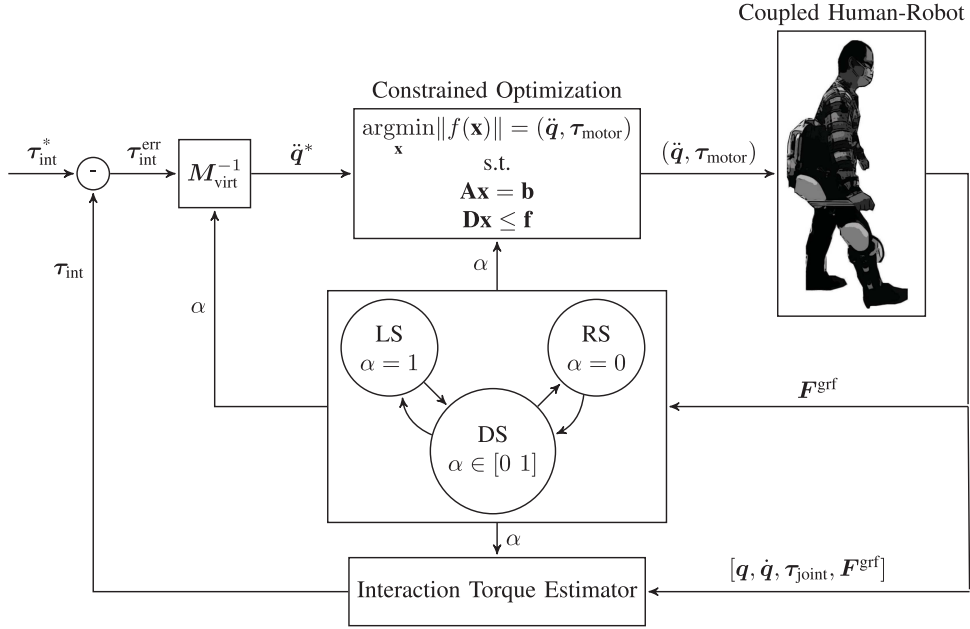


Fig. 4. Schematic of the interaction force controller.

in Table IV. The virtual inertia of the backpack is relatively large to allow better control performance at the leg segments.

2) *Constrained Optimization*: While the desired acceleration  $\ddot{q}^*$  in (21) is a 5-D vector, the exoskeleton has only four actuated joints. Therefore, it is not possible to perfectly track the desired generalized accelerations calculated by the virtual mass controller. Moreover, the maximum torque, power, and velocity of the motors bring additional limitations. To track the desired generalized acceleration as accurately as possible under physical and safety constraints, we use real-time constrained optimization with OSQP library [36] to solve for  $\mathbf{x} = [\ddot{\mathbf{q}}^\top, \boldsymbol{\tau}_{\text{motor}}^\top]^\top \in \mathbb{R}^9$ , where  $\boldsymbol{\tau}_{\text{motor}}$  is a vector of torque commands sent to the motor drivers

$$\begin{aligned} \min_{\mathbf{x}} \quad & \|f(\mathbf{x})\| \\ \text{s.t.} \quad & \mathbf{A}\mathbf{x} = \mathbf{b} \\ & \mathbf{D}\mathbf{x} \leq \mathbf{f}. \end{aligned} \quad (22)$$

The objective function  $\|f(\mathbf{x})\|$  is the 2-norm of the difference between the actual and desired generalized accelerations

$$f(\mathbf{x}) = [\mathbb{I}_{5 \times 5}, \mathbb{0}_{5 \times 4}] \mathbf{x} - \ddot{\mathbf{q}}^*. \quad (23)$$

The equality constraint ensures that optimized variables satisfy the equation of motion of the corresponding gait state under physical limits

$$\begin{aligned} \mathbf{A} &= \mathbf{A}_{\text{EOM}} = [\mathbf{M}_i, -\mathbf{S}^\top] \\ \mathbf{b} &= \mathbf{b}_{\text{EOM}} = [-\mathbf{b}_i - \mathbf{g}_i + \boldsymbol{\tau}_{\text{int}} + \mathbf{S}^\top \boldsymbol{\tau}_{\text{friction}}] \end{aligned} \quad (24)$$

where  $i \in \{\text{ls, rs, ds}\}$ . Inequality constraints arise from physical and safety constraints on motor torque, power, and velocity. Motor torque and power constraints are presented in (25) and (26),

respectively,

$$\begin{aligned} \mathbf{D}_{\boldsymbol{\tau}_{\max}^+} &= [0_{4 \times 5}, \mathbb{I}_{4 \times 4}], \mathbf{f}_{\boldsymbol{\tau}_{\max}^+} = \boldsymbol{\tau}_{\max} \\ \mathbf{D}_{\boldsymbol{\tau}_{\max}^-} &= [0_{4 \times 5}, -\mathbb{I}_{4 \times 4}], \mathbf{f}_{\boldsymbol{\tau}_{\max}^-} = \boldsymbol{\tau}_{\max} \end{aligned} \quad (25)$$

$$\begin{aligned} \mathbf{D}_{\mathcal{P}_{\max}^+} &= [0_{4 \times 5}, \mathbb{I}_{4 \times 4}], \mathbf{f}_{\mathcal{P}_{\max}^+} = \frac{\mathcal{P}_{\max}}{|\dot{\mathbf{q}}|} \\ \mathbf{D}_{\mathcal{P}_{\max}^-} &= [0_{4 \times 5}, -\mathbb{I}_{4 \times 4}], \mathbf{f}_{\mathcal{P}_{\max}^-} = \frac{\mathcal{P}_{\max}}{|\dot{\mathbf{q}}|} \end{aligned} \quad (26)$$

where  $\boldsymbol{\tau}_{\max} = 80 \text{ Nm}$  and  $\mathcal{P}_{\max} = 100 \text{ W}$  are the maximum allowable torque and power of the motors, respectively, and the superscripts + and - are used to indicate the maximum and minimum limits, respectively.

The joint velocity constraint is converted to an acceleration constraint, such that the joint speed at the next time step will not exceed maximum limits

$$\begin{aligned} \mathbf{D}_{\dot{\mathbf{q}}^+} &= [0_{4 \times 1}, \mathbb{I}_{4 \times 4}, 0_{4 \times 4}], \mathbf{f}_{\dot{\mathbf{q}}^+} = \frac{\dot{\mathbf{q}}_{\max} - \dot{\mathbf{q}}}{\Delta t} \\ \mathbf{D}_{\dot{\mathbf{q}}^-} &= [0_{4 \times 1}, -\mathbb{I}_{4 \times 4}, 0_{4 \times 4}], \mathbf{f}_{\dot{\mathbf{q}}^-} = \frac{\dot{\mathbf{q}}_{\max} + \dot{\mathbf{q}}}{\Delta t} \end{aligned} \quad (27)$$

where  $\dot{\mathbf{q}}_{\max} = 3.0 \text{ rad/s}$  and  $\Delta t = 0.003 \text{ s}$  is the control loop period. Individual  $\mathbf{D}$  matrices and  $\mathbf{f}$  vectors in (25)–(27) are vertically stacked to obtain the overall  $\mathbf{D}$  matrix and  $\mathbf{f}$  vector in (22). The controller is illustrated in Fig. 4.

Because we have only a single objective function for this task, a constrained optimization suffices. In the case of multiple objectives with different priorities, a hierarchical optimization framework could be applied [37], [38]. This allows optimization of lower-priority tasks using freedoms in the design vector that do not affect the objective functions of higher-priority tasks.

#### IV. EXPERIMENTAL VALIDATION

Three healthy subjects (one male, two female,  $71.6 \pm 12.9$  kg,  $174 \pm 1.7$  cm,  $29 \pm 2.6$  years) participated in this study to test the proposed interaction torque controller. The link lengths of the exoskeletons were adjusted for each participant so that they were comfortable and their joints were aligned with the exoskeleton's. The adjusted link lengths were also entered into software for automatic modification of the dependent parameters such as  $M$ ,  $b$ , and  $g$ . None of the subjects had used a lower limb exoskeleton before this study. At the beginning of the experiment, subjects were allowed about two minutes of walking with the exoskeleton on a treadmill for familiarization. Subjects were asked to always hold the hand-rails on the sides of the treadmill for safety and to balance in the frontal plane.

We tested the haptic rendering capabilities for zero desired interaction torque under three conditions and nonzero desired interaction torques under two different conditions. In addition to the proposed controller (WECC), the following two conditions were tested:

1) *No-Drive*: A passive exoskeleton with disassembled drives was used. This allowed us to have a baseline condition where the main sources of friction and inertia (apparent rotor inertia) are eliminated. Subjects still felt the weight of the exoskeleton, however.

2) *Simplified*: The exoskeleton legs are modeled and controlled as independent double pendulums. Equations (10) and (20) were used to estimate the interaction torques and follow desired accelerations, respectively. The details of this controller are presented in Appendix A.

The institutional review board of Northwestern University approved this study (STU00212684), and all procedures were in accordance with the Declaration of Helsinki.

##### A. Evaluation of Transparency

Haptic transparency was tested for our proposed WECC method, the double-pendulum-based simplified controller, and the passive no-drive condition. For the WECC and simplified controller, zero desired interaction torque was commanded for each generalized coordinate. Each condition was tested for three trials of around 65 s walking on a treadmill with a speed of 1.1 km/h. The first five seconds of data were discarded to focus on steady-state walking. A relatively slow speed was selected due to the usual walking training speeds in physical rehabilitation settings for individuals with stroke or incomplete spinal cord injury and the joint velocity limits of 3.2 rad/s of the ExoMotus-X2 exoskeleton. Trials of the WECC and simplified controllers were performed in a randomized order for each subject. All trials of the passive no-drive condition were performed consecutively for practical reasons, as this condition requires a different exoskeleton with disassembled drives. A metronome was played at 40 bpm, and subjects were asked to synchronize their heel strikes with the beats of the metronome to have similar step lengths between subjects and trials.

Human-exoskeleton interaction torques and muscle activity were used to assess transparency performance.

TABLE V  
VIRTUAL STIFFNESS AND DAMPING VALUES USED FOR HAPTIC RENDERING EVALUATION

Joint	Leg Phase	$k_i$ [Nm/rad]	$c_i$ [Nms/rad]	$q_i^*$ [degrees]
Hip	Stance	50	10	25
Hip	Swing	30	6	25
Knee	Stance	30	6	-45
Knee	Swing	25	5	-45

##### B. Evaluation of Haptic Rendering

We tested the interaction torque rendering capabilities of the WECC controller and the simplified controller when the desired interaction torques are generated by virtual springs and dampers at the joints

$$\tau_{\text{int}}^* = \mathbf{K}(\mathbf{q} - \mathbf{q}^*) + \mathbf{C}\dot{\mathbf{q}} \quad (28)$$

where  $\mathbf{q}^*$  is the neutral position vector of the virtual springs and  $\mathbf{K} \in \mathbb{R}^{5 \times 5}$  and  $\mathbf{C} \in \mathbb{R}^{5 \times 5}$  are diagonal stiffness and damping matrices, respectively. A constant  $q_i^*$  was used at each joint  $i$ , and the desired interaction torque at the backpack was set to zero by assigning  $K_0$  and  $C_0$  to zero. The constant neutral angles were chosen, such that the desired interaction torques have a similar magnitude in both directions. Since the motion of a leg during stance is slower and has a smaller range, larger stiffness and damping constants were used for stance phases than for swing phases. The magnitudes of the stiffness and damping were chosen during pilot trials, such that the rendered torque is significant but does not prevent the user from walking at the requested speed. The diagonal values of the stiffness ( $k_i$ ) and damping ( $c_i$ ) matrices, as well as  $\mathbf{q}^*$ , are presented in Table V. To avoid discontinuities in the desired interaction torque during stance to swing transitions, the desired interaction torque was low-pass filtered with a cutoff frequency of 5 Hz.

##### C. Data Recording and Analysis

Joint positions, velocities, and interaction torques were recorded during all trials. The exoskeleton without drives is instrumented with IMUs (Tech-IMU V4, Technaid, Spain) at each link to measure joint motions, which are used in interaction torque calculation. Because IMUs were placed on the exoskeleton and not on the user, they were not affected by possible human-robot joint misalignment. All exoskeleton data were collected at 333 Hz.

Nine bipolar electromyography (EMG) electrodes (MA400 EMG Systems, Motion Lab Systems, USA) were placed on the belly of the following muscles for the evaluation of transparency experiments: rectus femoris (RF), vastus lateralis (VL), vastus medialis (VM), biceps femoris (BF), semitendinosus (ST), medial gastrocnemius (MG), lateral gastrocnemius (LG), and soleus (SOL). The electrodes were placed only on the left leg and not removed between trials. EMG data were recorded at 1500 Hz. The raw EMG signals were first bandpass filtered between 20 and 500 Hz with a sixth-order Butterworth filter. Then, a notch filter between 59 and 61 Hz was applied to reduce noise due to power line interference. Finally, the signals were low-pass filtered at 10 Hz after full-wave rectification. Processed EMG

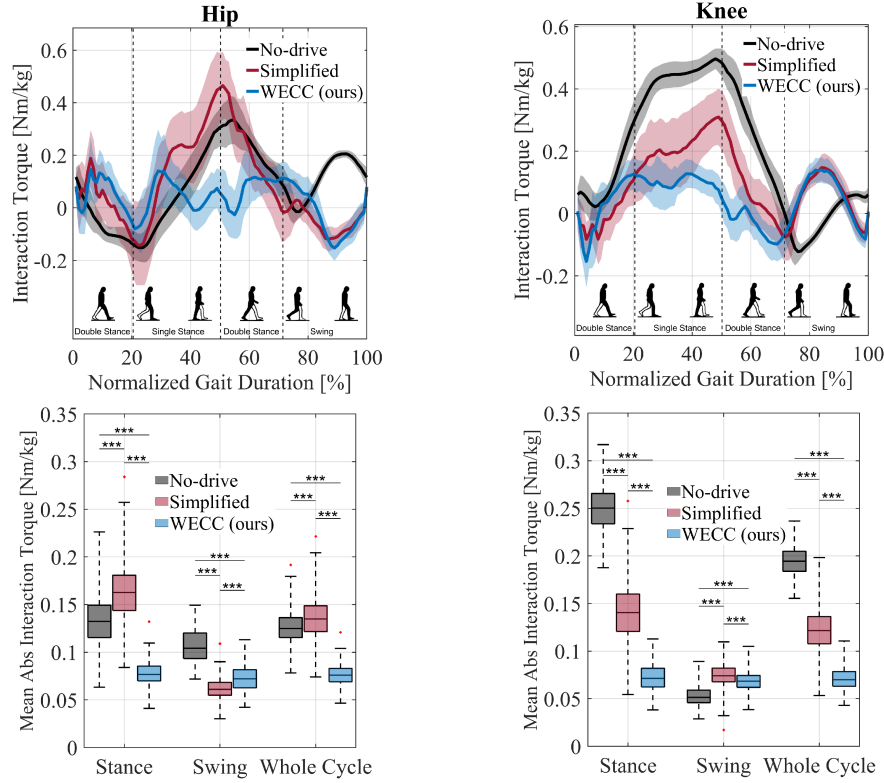


Fig. 5. Interaction torques between the human and exoskeleton during transparency trials. The figures on the top row show the interaction torques versus normalized gait duration for a representative subject. The data includes every step of both legs, and the shaded area represents  $\pm$  standard deviation. On the bottom row, the box and whisker plots of the mean absolute interaction torques during the stance phase, swing phase, and the whole gait cycle are presented. Mean absolute values of the corresponding phase at each step of both legs of all three subjects are used as a data point after removing the intersubject variability in box and whisker plots ( $N \approx 320$ ). \*\*\* indicates  $p < 0.001$  from Tukey's HSD test.

signals were normalized with respect to the mean of the no-drive condition for each subject independently. For one subject, RF recordings were not successfully collected due to sensor failure.

Exoskeleton-based measurements and processed EMG readings were windowed between the heel strikes of the corresponding leg. Windowed data from the same joint on both legs and three subjects were lumped together for each condition. The mean absolute value of the whole cycle and only stance or swing phases for each gait cycle were used as sample points and visualized in the corresponding box plots in the Results section.

To test the difference in means between each condition for each measure (i.e., interaction torque, muscle activity), we used two-way ANOVA analyses with condition and subject as fixed effects, as well as the interaction between these variables. Post-hoc comparisons were made using Tukey's honestly significant difference (HSD) test for transparency experiments comparing the three conditions. A  $p$ -value of 0.05 was used to accept or reject null hypotheses. Though the effects of intersubject variability were included in the ANOVA analyses, we only present the ANOVA results and posthoc comparisons for the condition, as the focus of this article is controller development. To ensure consistency with ANOVA analyses and prevent the mixing of inter and intrasubject variability, we removed the intersubject variability from the data presented in the box plots and tables in the following section. This is achieved by demeaning the data of

TABLE VI  
MEAN AND (STANDARD DEVIATION) OF THE INTERACTION TORQUES BETWEEN THE HUMAN AND EXOSKELETON AT THE HIP AND KNEE JOINTS DURING TRANSPARENCY EXPERIMENTS

Joint/Phase	No-drive (c <sub>1</sub> )	Simplified (c <sub>2</sub> )	WECC (c <sub>3</sub> )	<i>p</i>	Tukey's HSD
Hip/Stance	0.13 (0.03)	0.16 (0.03)	0.08 (0.01)	<0.001	c <sub>3</sub> < c <sub>1</sub> < c <sub>2</sub>
Hip/Swing	0.11 (0.02)	0.06 (0.01)	0.07 (0.01)	<0.001	c <sub>2</sub> < c <sub>3</sub> < c <sub>1</sub>
Hip/WC	0.13 (0.02)	0.14 (0.02)	0.08 (0.01)	<0.001	c <sub>3</sub> < c <sub>1</sub> < c <sub>2</sub>
Knee/Stance	0.25 (0.02)	0.14 (0.03)	0.07 (0.01)	<0.001	c <sub>3</sub> < c <sub>2</sub> < c <sub>1</sub>
Knee/Swing	0.001 (0.01)	0.07 (0.01)	0.07 (0.01)	<0.001	c <sub>1</sub> < c <sub>3</sub> < c <sub>2</sub>
Knee/WC	0.19 (0.02)	0.12 (0.02)	0.07 (0.01)	<0.001	c <sub>3</sub> < c <sub>2</sub> < c <sub>1</sub>

All values are expressed in Nm/kg. *p*-values for the effect of condition in the two-way ANOVA and significant posthoc comparisons are presented in the right columns.  
WC:Whole Cycle.

each condition/subject pair and subsequently adding the overall mean of each condition, including three subjects.

## V. RESULTS

### A. Transparency

Participants were able to follow the metronome, and there was no significant difference between the step time at different conditions (no-drive:  $1.49 \pm 0.06$  s, simplified:  $1.51 \pm 0.06$  s, WECC:  $1.50 \pm 0.06$  s). Interaction torques during the transparency trials, normalized by the body mass of each subject (units of Nm/kg), are presented in Fig. 5 and Table VI. Below we describe the

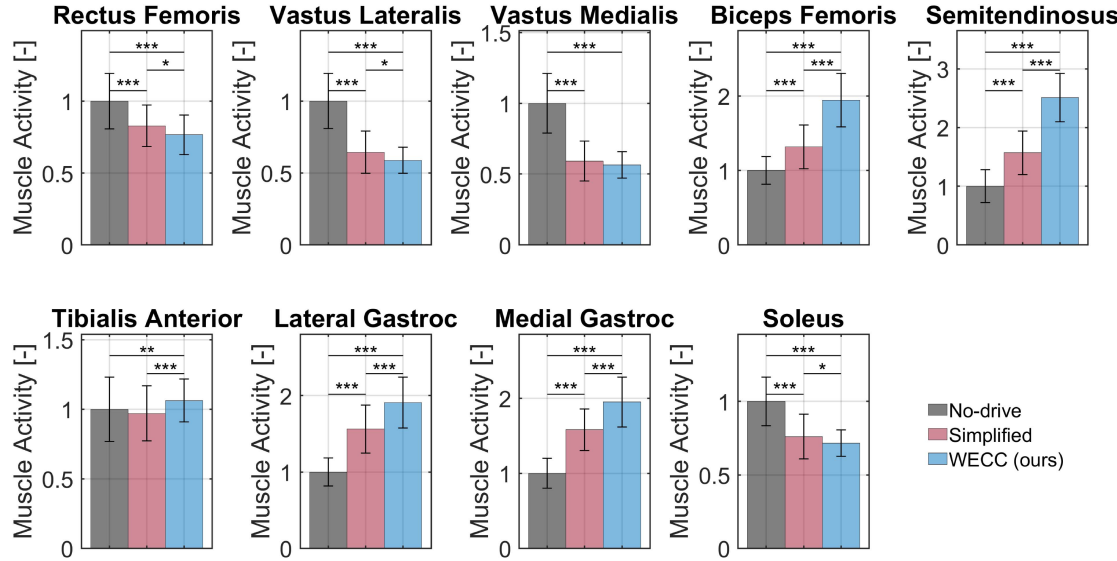


Fig. 6. Muscle activity during transparency experiments. Data are normalized with respect to the mean of the no-drive condition. Mean absolute values of the filtered EMG data averaged over the whole cycle at each step of all subjects are used after removing the intersubject variability as a data point in bar plots ( $N \approx 160$ ). \*, \*\*, and \*\*\* indicate  $p < 0.05, 0.01$ , and  $0.001$ , respectively, from Tukey's HSD test.

interaction torques during a leg's swing phase, its stance phase (both single stance and double stance unless otherwise noted), and its entire cycle.

The performance of the proposed WECC controller was consistent throughout the whole gait cycle with a mean absolute interaction torque around  $0.07 \pm 0.02$  Nm/kg both at the hip and knee joints during both stance and swing phases. The simplified controller resulted in a similar mean absolute interaction torque during the swing phase (difference of mean absolute interaction torques  $\Delta \leq 0.01$  Nm/kg) but significantly higher mean absolute interaction torque of 0.16 and 0.14 Nm/kg at the hip and knee joints, respectively, during the stance phase. During the stance phase, higher interaction torques were observed for the no-drive condition than for WECC at both the hip ( $\Delta \geq 0.06$  Nm/kg,  $p < 0.001$ ) and knee ( $\Delta \geq 0.17$  Nm/kg,  $p < 0.001$ ) joints. During the swing phase, the no-drive condition resulted in significantly higher interaction torques at the hip joint ( $\Delta \geq 0.05$  Nm/kg,  $p < 0.001$ ) and similar interaction torques at the knee joint ( $\Delta \approx 0.01$  Nm/kg) compared with the proposed WECC method. Average transparency performance during the whole cycle was best for the WECC controller, with mean absolute interaction torques of  $0.076 \pm 0.011$  Nm/kg and  $0.071 \pm 0.011$  Nm/kg at the hip and knee joints, respectively. The simplified controller achieved better mean absolute interaction torque than the no-drive condition at the knee joint ( $\Delta \approx 0.07$  Nm/kg) averaged over the whole gait cycle. At the hip joint, both performances were similar with a mean interaction torque difference around 0.01 Nm/kg.

Fig. 6 and Table VII show the muscle activity of the various muscles during the transparency trials. It is seen that muscles responsible for hip flexion (RF) and knee extension (RF, VL, and VM) had the lowest activation with the WECC controller and highest with the passive no-drive condition. On the other hand, our controller resulted in the most activity, and the no-drive condition resulted in the least activity, for the muscles responsible

TABLE VII  
MEAN AND (STANDARD DEVIATION) OF MUSCLE ACTIVITIES DURING  
TRANSPARENCY EXPERIMENTS, NORMALIZED WITH RESPECT TO THE MEAN  
OF THE NO-DRIVE CONDITION

Muscle	No-drive ( $c_1$ )	Simplified ( $c_2$ )	WECC ( $c_3$ )	$p$	Tukey's HSD
RF	1 (0.19)	0.83 (0.14)	0.77 (0.14)	<0.001	$c_3 < c_2 < c_1$
VL	1 (0.19)	0.64 (0.15)	0.59 (0.09)	<0.001	$c_3 < c_2 < c_1$
VM	1 (0.21)	0.59 (0.14)	0.56 (0.09)	<0.001	$c_1 > c_2, c_3$
BF	1 (0.19)	1.32 (0.29)	1.94 (0.36)	<0.001	$c_1 < c_2 < c_3$
ST	1 (0.28)	1.57 (0.37)	2.51 (0.41)	<0.001	$c_1 < c_2 < c_3$
TA	1 (0.23)	0.97 (0.20)	1.06 (0.15)	<0.001	$c_3 > c_1, c_2$
LG	1 (0.18)	1.56 (0.31)	1.91 (0.33)	<0.001	$c_1 < c_2 < c_3$
MG	1 (0.20)	1.58 (0.28)	1.95 (0.33)	<0.001	$c_1 < c_2 < c_3$
SOL	1 (0.17)	0.76 (0.15)	0.72 (0.09)	<0.001	$c_3 < c_2 < c_1$

p-values for the effect of condition in the two-way ANOVA and significant post-hoc comparisons are presented in the right columns.

for hip extension and knee flexion (BF and ST). Furthermore, the SOL muscle, responsible for ankle plantar flexion, was used the least with the WECC controller and the most under the no-drive condition. In contrast, LG and MG muscles, responsible for knee flexion and ankle plantar flexion, had the highest activation with the WECC controller and the lowest under the no-drive condition.

### B. Haptic Rendering

Properties of the rendered virtual spring-damper elements shown in Table V resulted in the desired interaction torques presented in Fig. 7. The figure includes data from the joints of both legs and three subjects. Desired interaction torques vary in the range  $\pm 15$  Nm during the gait cycle for all subjects. There was no significant difference between the step times at different conditions (Simplified:  $1.32 \pm 0.13$  s, WECC:  $1.31 \pm 0.13$  s). The demonstration of the haptic rendering performance of the WECC control is also presented in this video.<sup>3</sup>

<sup>3</sup>Video is available online at <https://tinyurl.com/ExoHapticRendering>

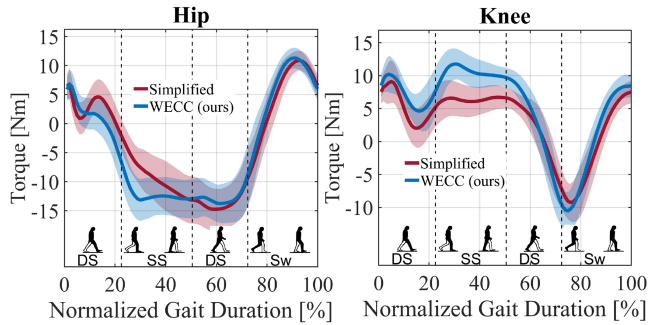


Fig. 7. Desired interaction torque due to the rendered spring damper elements.

TABLE VIII  
MEAN AND (STANDARD DEVIATION) OF THE INTERACTION TORQUE ERROR  
BETWEEN THE HUMAN AND EXOSKELETON AT HIP AND KNEE JOINTS DURING  
HAPTIC RENDERING EXPERIMENTS

Joint/Phase	Simplified (c <sub>2</sub> )	WECC (c <sub>3</sub> )	p
Hip/Stance	0.12 (0.02)	0.05 (0.01)	<0.001
Hip/Swing	0.04 (0.01)	0.04 (0.01)	0.49
Hip/WC	0.10 (0.02)	0.05 (0.01)	<0.001
Knee/Stance	0.21 (0.02)	0.05 (0.01)	<0.001
Knee/Swing	0.04 (0.01)	0.05 (0.01)	<0.001
Knee/WC	0.17 (0.02)	0.05 (0.01)	<0.001

All values are expressed in Nm/kg. p-values for the effect of condition in the two-way ANOVA are presented in the right column. WC:Whole Cycle.

The rendering performance of our proposed WECC controller and the simplified controller are shown in Fig. 8 and Table VIII. Similar to the performance of transparency trials, our controller's interaction torque tracking error was consistent throughout the whole cycle. On the other hand, the simplified controller resulted in a large peak of interaction torque errors on both joints near the end of the single stance state.

The WECC controller resulted in a normalized mean absolute interaction torque error of  $0.049 \pm 0.008$  Nm/kg and  $0.039 \pm 0.008$  Nm/kg at the hip joint during the stance and swing phases, respectively. The simplified controller resulted in a similar mean absolute error during the swing phase both at the hip and knee joints ( $\Delta \leq 0.01$  Nm/kg). On the other hand, the average absolute interaction torque error was significantly larger during the stance phase both at the hip ( $\Delta \geq 0.07$  Nm/kg,  $p < 0.05$ ) and knee ( $\Delta \geq 0.16$  Nm/kg,  $p < 0.05$ ) joints. Averaged over the whole cycle, the WECC controller resulted in an error of  $0.050 \pm 0.006$  Nm/kg for both hip and knee joints. The errors of the simplified controller were significantly larger both at the hip ( $\Delta \geq 0.05$  Nm/kg,  $p < 0.05$ ) and knee joints ( $\Delta \geq 0.12$  Nm/kg,  $p < 0.05$ ).

## VI. DISCUSSION

### A. Interaction Torque Tracking

The simplified controller and the proposed WECC controller performed similarly during the swing phase for both joints in the transparency and haptic rendering trials, as shown in Figs. 5 and 8. Since the swing leg is not affected by the weight of the backpack and the other leg, the two-link simplified model is sufficient and results in accurate interaction torque

estimation and motor torque calculation for the swing leg. On the other hand, the simplified controller failed to render the desired interaction torques for the stance leg. This is because the model does not consider whole-body dynamics, resulting in incorrect interaction torque estimation for the stance leg. For the simplified controller, subjects feel additional torques on their joints due to the uncompensated weight of the exoskeleton. The calculation of dynamical parameters and the differences between the two approaches are presented in Appendixes B and C. As the proposed WECC controller uses whole-body dynamics and considers physical limitations, the interaction torque tracking performance was consistent throughout the entire gait cycle.

The most transparent performance at the knee joint was obtained during the swing phase of the no-drive condition. This is because the weight of the shank is insignificant, and there is low friction and no apparent rotor inertia. Because of the larger inertia, the no-drive condition results in more interaction torque at the hip joint compared with the active controllers, where the weight of the leg is compensated. The highest amount of interaction torque was observed for the stance leg under the no-drive condition, as the stance leg of the subject needs to overcome the torques due to the weight of the exoskeleton's stance leg, swing leg, and backpack.

The proposed method uses the exoskeleton model to estimate interaction torque and control acceleration to track the desired interaction torque. Considering the model-based dynamics based on the gait state results in consistent performance throughout the whole gait cycle. This model-based approach depends on an accurate dynamic model. Thanks to CAD tools, this is not difficult to obtain. Accurate friction modeling is more challenging. Performance can be improved by 1) using a more accurate friction model and 2) estimating joint accelerations in real time and implementing an inner acceleration control loop to compensate modeling errors. Estimating real-time accelerations also allows considering the neglected inertial terms in interaction torque estimation. In our postexperiment analyses, we observed that the mean absolute values of the neglected inertial torques were around 14% of the total dynamical forces.

### B. Muscle Activity

The muscles responsible for hip flexion (RF) and knee extension (RF, VL, and VM) were activated the least with the proposed WECC controller and the most with the passive no-drive condition during the transparency trials. This is mainly due to the accurate compensation of the exoskeleton dynamics for the WECC controller.

The opposite trend was observed for the muscles responsible for hip extension and knee flexion (BF and ST). These muscles were activated more with the WECC controller than for the no-drive and simplified conditions. This is expected for BF and ST, remembering that the transparency goal for WECC is zero interaction torque, not assist. The uncompensated weight of the exoskeleton in the no-drive and simplified conditions results in significant hip-extension torque assist during early double stance, as shown in Fig. 9, by the large positive power flow from the exoskeleton to the user.

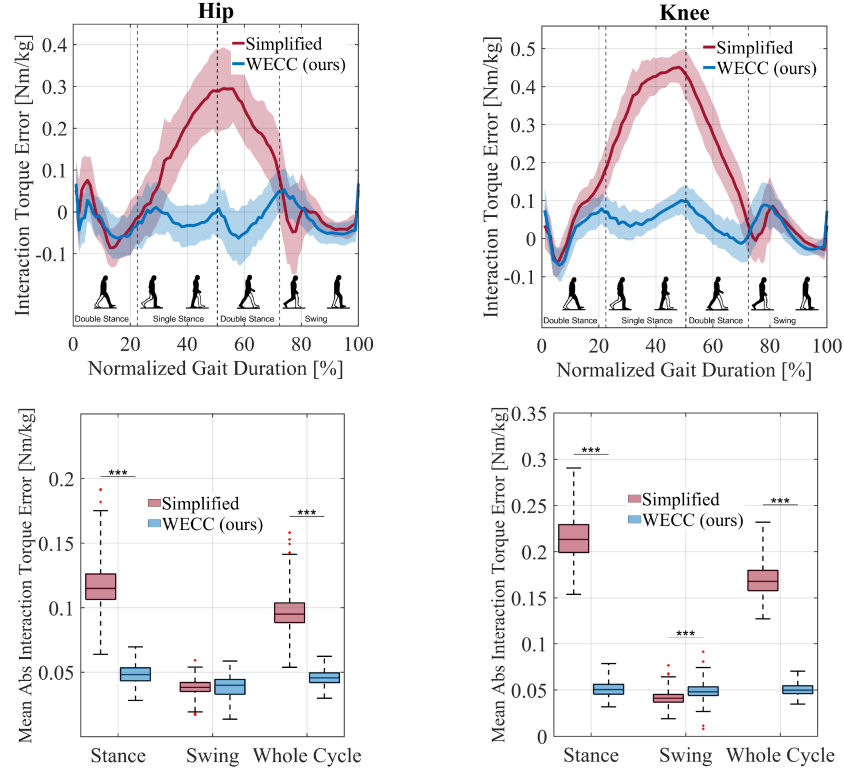


Fig. 8. Interaction torque error during haptic rendering trials. The figures on the top row show the interaction torque error versus normalized gait duration for a representative subject. The data includes every step of both legs, and the shaded area represents  $\pm$  standard deviation. On the bottom row, the box and whisker plots of the mean absolute interaction torque error during the stance phase, swing phase, and the whole gait cycle are presented. Mean absolute values of the corresponding phase at each step of both legs of all three subjects are used after removing the intersubject variability as a data point in box and whisker plots ( $N \approx 370$ ). \*\*\* indicates  $p < 0.001$  from ANOVA results.

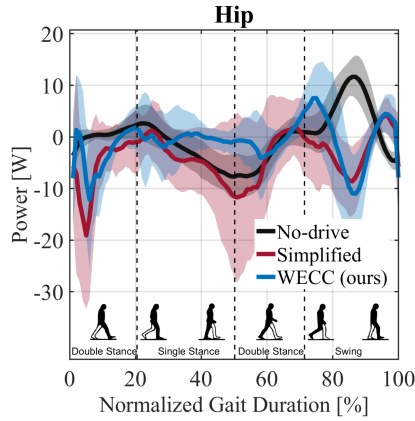


Fig. 9. Hip interaction power during transparency experiments. Positive and negative values indicate resistance and assistance to the human, respectively.

The gastrocnemius muscles (LG and MG), which cause ankle plantar flexion and knee flexion, were activated most with the WECC controller and least with the no-drive condition. On the other hand, an opposite trend was observed for the SOL muscle, which causes only ankle plantar flexion. High interaction torques in the knee flexion direction (positive direction in Fig. 5) for the simplified and no-drive conditions leads to less gastrocnemius activity in these conditions. This explains the different trend between gastrocnemius and SOL muscles.

### C. Overground Walking

The proposed method requires the ratios of the vertical GRF and the direction of GRF in the sagittal plane. While we used external force plates under the treadmill, these terms can also be obtained using wearable sensors or sensors instrumented onto the exoskeleton. For example, the ratio of the vertical forces can be measured with simple and cost-effective force sensitive resistor (FSR) sensors or pressure pads.

It is relatively harder to measure the horizontal GRF because instrumented insoles usually provide only vertical forces. One can implement force sensors that provide two-directional force measurements [39] or indirectly estimate the anterior-posterior force assuming the foot does not slip on the ground [40] or using a model and estimated accelerations [41]. Because accelerations and decelerations are small for slow gait speeds, it is also possible to assume horizontal GRF to be near zero. The effect of this assumption on the interaction torque estimation was tested on the collected experimental data from all subjects during WECC conditions. Fig. 10 shows that the interaction torque estimates are changed little by this assumption.

The supplementary video includes preliminary overground tests with FSR pads implemented at the bottom of the feet while assuming horizontal forces to be near zero. The user in the video climbs over a small step and walks forward and backward. We also conducted a pilot test where a user walked a distance of 4.5 m four times with each controller (WECC and simplified) in

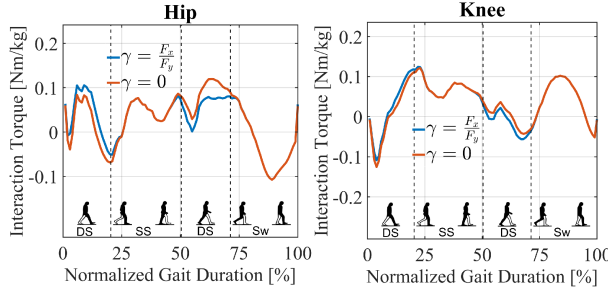


Fig. 10. Mean interaction torque estimation of all subjects during the all WECC trials using the direction of the GRF ( $\gamma = F_x/F_y$ ) and assuming horizontal GRF is negligible ( $\gamma = 0$ ).

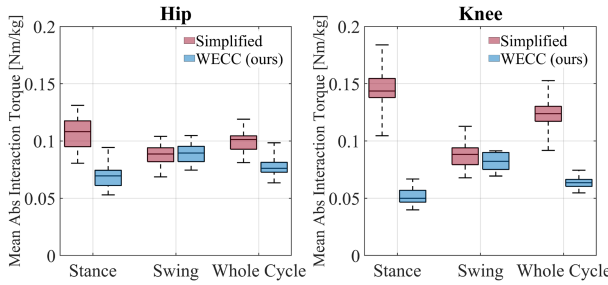


Fig. 11. Mean absolute interaction torques during the pilot overground tests.

haptic transparent mode, while holding onto parallel bars. We observed similar trends between this overground walking test and the treadmill experiments. Mean absolute interaction torque results are presented in Fig. 11. In the stance phase, the WECC controller resulted in a 35% and 65% decrease in mean absolute interaction torque at the hip and knee joints, respectively, compared with the simplified controller. The performance of the two controllers was similar in the swing phase (difference less than 1% and 5.5% for hip and knee, respectively).

## VII. CONCLUSION

We have presented the WECC controller to measure and control the interaction torques between a user and a floating base hip-knee exoskeleton that contacts the ground. The WECC controller calculates the interaction torques using joint torque measurements and gait state information. The desired joint interaction torques are achieved by using a virtual mass controller together with a constrained optimization scheme that considers the whole-exoskeleton dynamics, physical limits, and safety constraints. The performance of the WECC controller was compared in terms of transparency and spring-damper haptic rendering with a commonly-used simplified double-pendulum model where the legs are modeled independent of one another. WECC control resulted in consistent interaction torque tracking during the whole gait cycle for both zero and nonzero desired interaction torques, whereas the simplified controller failed to track desired interaction torques during the stance phase.

Future improvements to WECC control could include explicit modeling of joint limits in the dynamic model, particularly because the knee joint gets close to the physical limit during the gait cycle. This will improve the accuracy of the forward

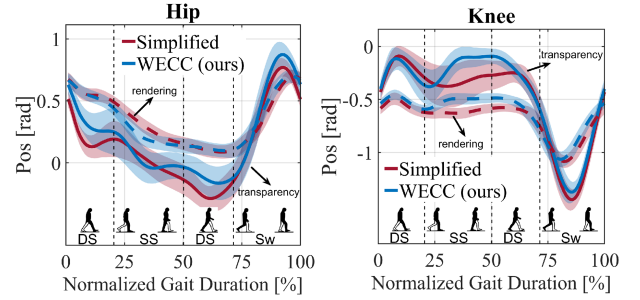


Fig. 12. Hip and knee joint positions for simplified and WECC controller during transparency (solid line) and haptic rendering experiments (dashed line) for a representative subject.

model and, therefore, the tracking of the optimized accelerations. Moreover, an inner acceleration loop to compensate for the modeling inaccuracies, using additional IMUs or reinforcement learning-based strategies [42] for online optimization of system parameters, may be options to improve the current results.

A limitation when comparing interaction torques between different controllers arises from the challenge of obtaining ground-truth data. Reflected interaction torques are influenced by forces at each contact point, necessitating the installation of force/torque (F/T) sensors at every contact point for the measurement of these interaction torques. Because this is practically challenging, we used the whole-body dynamics of the exoskeleton to estimate the interaction torques as accurately as possible while comparing different controller performances. More accurate comparisons could be possible with an experimental setup where the contact points are kept at a minimum and all are sensorized.

The WECC controller can potentially be used to adjust the interaction torques to assist a user in overground walking, to resist for training in a clinical setting, or to provide haptic transparency on lower limb exoskeletons with feet. Commercial versions of this type of exoskeleton are usually heavy, have high friction, and do not have force-torque sensors. Consequently, they have been utilized primarily for position control rather than accurate interaction force control. The proposed WECC control overcomes these limitations and is especially beneficial for heavy lower limb exoskeletons where the whole-body dynamics need to be compensated. In future studies, this infrastructure will be used to investigate the effects of dyadic haptic interaction on performance and learning for complex multiDOF lower limb motions [43], [44], [45].

## APPENDIX A SIMPLIFIED CONTROLLER

For the simplified controller, the legs are modeled as two-link chains independent of each other. This model is used to estimate interaction torques as in 20. Since an optimization scheme considering physical limits is not implemented in the related works in Table I, we do not use one for the simplified controller. Instead, 10 is used as the forward model to track the desired acceleration commands sent by the virtual mass controller. The

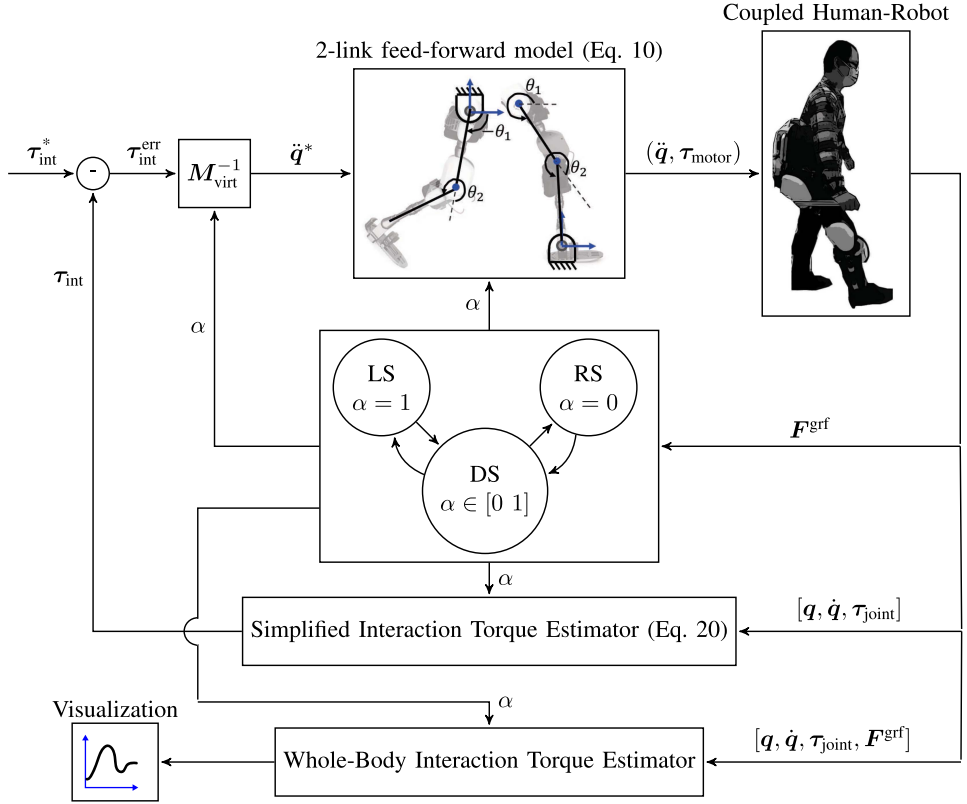


Fig. 13. Schematic of the interaction force controller used in the simplified condition.

same controller gains for thigh and shank presented in Table IV are used. The simplified interaction torque estimation is used in the control loop; however, the presented interaction torque results are calculated using the whole-body model to compare the results between conditions. The overall control structure is presented in Fig. 13. The control structure runs independently for each leg.

## APPENDIX B CALCULATION OF THE DYNAMIC PARAMETERS

The mass matrix  $M$ , Coriolis vector  $b$ , and gravitational vector  $g$  are calculated during single stance in both WECC and the simplified model as

$$M_i = \sum_{n \in N_i} J_{S,i}^n \top m_n J_{S,i}^n + J_{R,i}^n \top \Theta_n J_{R,i}^n \quad (29)$$

$$b_i = \sum_{n \in N_i} J_{S,i}^n \top m_n \dot{J}_{S,i}^n \dot{q} + J_{R,i}^n \top \Theta_n \dot{J}_{R,i}^n \dot{q} \quad (30)$$

$$g_i = - \sum_{n \in N_i} J_{y,i}^n \top m_n g \quad (31)$$

where  $i \in \{ls, rs, st, \text{and } sw\}$ . The subscripts  $i = ls$  and  $i = rs$  correspond to left stance and right stance for the whole-body model, and  $i = st, i = sw$  correspond to the state of a single leg being stance or swing for the simplified model as explained in Section II-B. The index  $n$  corresponds to the links of the exoskeleton in the following order: Backpack ( $n = 1$ ), stance thigh

( $n = 2$ ), stance shank and foot ( $n = 3$ ), swing thigh ( $n = 4$ ), and swing shank and foot ( $n = 5$ ). For the whole-body model, all links are considered; therefore,  $N_{ls} = N_{rs} = \{1, 2, 3, 4, 5\}$ . On the other hand, the simplified model considers the legs separately; therefore,  $N_{st} = \{2, 3\}$  and  $N_{sw} = \{4, 5\}$ . The mass and mass moment of inertia at the CoM of each link are represented by  $m_n$  and  $\Theta_n$ , respectively. The translational and rotational Jacobian of the CoM of each link are shown by  $J_{S,i}^n$  and  $J_{R,i}^n$ , respectively. It is important to note that these Jacobians are calculated depending on the model and gait state (i.e.,  $i$ ). For the whole-body model,  $J_{S,ls-rs}^n \in \mathbb{R}^{2 \times 5}$  and  $J_{R,ls-rs}^n \in \mathbb{R}^{1 \times 5}$ . For the simplified model,  $J_{S,st-sw}^n \in \mathbb{R}^{2 \times 2}$  and  $J_{R,st-sw}^n \in \mathbb{R}^{1 \times 2}$ . The variable  $J_{y,i}^n$  is the vertical component of the translational Jacobian.

## APPENDIX C DIFFERENCE BETWEEN INTERACTION TORQUE ESTIMATION USING SIMPLIFIED AND WECC MODELS

Due to the weight of the ExoMotus-X2 exoskeleton, gravitational torques  $g$  have the largest contribution to the interaction torque. Therefore, the difference of  $g$  between the whole-body and simplified model is investigated in this section.

The respective subsets of the whole-body Jacobians of the stance and swing CoMs are equal to the simplified stance and swing Jacobians

$$\begin{aligned} J_{y,i}^n[2 : 3] &= J_{y,st}^n & \forall n \in \{2, 3\}, i \in \{ls, rs\} \\ J_{y,i}^n[4 : 5] &= J_{y,sw}^n & \forall n \in \{4, 5\}, i \in \{ls, rs\} \end{aligned} \quad (32)$$

where the notation [a:b] denotes the subset of elements from index a (inclusive) to index b (inclusive).

Using (31) and (32), the difference between the gravitational torques on the swing leg in the whole-body model and the simplified swing model is

$$\mathbf{g}_i[4 : 5] - \mathbf{g}_{sw} = \sum_{n \in 1, 2, 3} -\mathbf{J}_{y,i}^n[4 : 5]m_n g, \quad i \in \{\text{ls}, \text{rs}\}. \quad (33)$$

The state of the swing leg or backpack does not affect the CoM positions on the stance leg with respect to the stance ankle. Therefore

$$\mathbf{J}_{y,i}^n[4 : 5] = 0_{1 \times 2} \quad \forall n \in \{1, 2, 3\}, i \in \{\text{ls}, \text{rs}\}. \quad (34)$$

This leads to

$$\begin{aligned} \sum_{n \in 1, 2, 3} -\mathbf{J}_{y,i}^n[4 : 5]m_n g &= 0 \\ \Rightarrow \mathbf{g}_i[4 : 5] &= \mathbf{g}_{sw}, \quad i \in \{\text{ls}, \text{rs}\} \end{aligned} \quad (35)$$

which shows the gravitational torques of the swing leg for the whole-body model are equivalent to the gravitational torques of the simplified swing model.

On the other hand, using (31) and (32), the difference between the gravitational torques on the stance leg in the whole-body model and the simplified stance model is

$$\mathbf{g}_i[2 : 3] - \mathbf{g}_{st} = \sum_{n \in 1, 4, 5} -\mathbf{J}_{y,i}^n[2 : 3]^T m_n g \quad i \in \{\text{ls}, \text{rs}\} \quad (36)$$

which shows the simplified stance gravitational torque has an error proportional to the weight of the backpack and swing legs. For heavy exoskeletons, such as the ExoMotus-X2, this error results in significant inaccuracy in interaction torque estimation.

## APPENDIX D

### DOUBLE STANCE EQUATION OF MOTION

Equation (3) can be written as an extension of both left stance dynamics ( $i = \text{ls}$ ) or right stance dynamics ( $i = \text{rs}$ ). Therefore

$$\mathbf{H}^\top \mathbf{X}_{ls} = \mathbf{H}^\top \mathbf{X}_{rs} \quad (37)$$

where  $\mathbf{X} \in \{\mathbf{M}\ddot{\mathbf{q}}, \mathbf{b}, \mathbf{g}\}$ . Multiplying (5)–(7) by  $\mathbf{H}^\top$  on the left

$$\begin{aligned} \mathbf{H}^\top \mathbf{X}_{ds} &= \mathbf{H}^\top (\alpha \mathbf{X}_{ls} + (1 - \alpha) \mathbf{X}_{rs}) \\ &= \mathbf{H}^\top \alpha \mathbf{X}_{ls} + \mathbf{H}^\top \mathbf{X}_{rs} - \mathbf{H}^\top \alpha \mathbf{X}_{rs} \\ &= \alpha (\mathbf{H}^\top \mathbf{X}_{ls} - \mathbf{H}^\top \mathbf{X}_{rs}) + \mathbf{H}^\top \mathbf{X}_{rs} \\ &= \mathbf{H}^\top \mathbf{X}_{rs} = \mathbf{H}^\top \mathbf{X}_{ls}. \end{aligned} \quad (38)$$

Therefore, the approximated dynamics of (5)–(7) satisfy the equation of motion (3).

The interpolation factor,  $\alpha$ , is chosen based on the torques needed to carry the weight of the exoskeleton during the double stance. Let  $\hat{\mathbf{g}}_{fly} \triangleq \mathbf{g}_{fly}[3 : 7]$  and  $\hat{\mathbf{J}}_{i,y} \triangleq \mathbf{J}_{i,y}[3 : 7]$ . Indexes from 3 to 7 correspond to the generalized coordinates during single and double stance (i.e.,  $\theta_0 \dots \theta_4$ ). The variable  $\mathbf{J}_{i,y}$  is the vertical ( $y$ ) component of the left ( $i = l$ ) or right ( $i = r$ ) ankle Jacobian in flight state.

The gravity vector during left and right stance can be expressed by the sum of the gravity vector during the flight state and the reflected joint torques due to the force on the stance foot

$$\begin{aligned} \mathbf{g}_{ls} &= \hat{\mathbf{g}}_{fly} - \hat{\mathbf{J}}_{l,y}^\top m_{exo} g \\ \mathbf{g}_{rs} &= \hat{\mathbf{g}}_{fly} - \hat{\mathbf{J}}_{r,y}^\top m_{exo} g \end{aligned} \quad (39)$$

where  $m_{exo} g$  is the total weight of the exoskeleton.

Similarly, the gravity vector during double stance is equal to the sum of the flight gravity vector and the reflected joint torques due to the vertical GRF on both legs

$$\begin{aligned} \mathbf{g}_{ds} &= \hat{\mathbf{g}}_{fly} - \hat{\mathbf{J}}_{l,y}^\top F_{l,y} - \hat{\mathbf{J}}_{r,y}^\top F_{r,y} \\ &= \alpha \mathbf{g}_{ls} + (1 - \alpha) \mathbf{g}_{rs}. \end{aligned} \quad (40)$$

Substituting (39) into (40)

$$\begin{aligned} \hat{\mathbf{g}}_{fly} - \hat{\mathbf{J}}_{l,y}^\top F_{l,y} - \hat{\mathbf{J}}_{r,y}^\top F_{r,y} \\ = \alpha \hat{\mathbf{g}}_{fly} - \alpha \hat{\mathbf{J}}_{l,y}^\top m_{exo} g + \hat{\mathbf{g}}_{fly} - \hat{\mathbf{J}}_{r,y}^\top m_{exo} g - \alpha \hat{\mathbf{g}}_{fly} \\ + \alpha \hat{\mathbf{J}}_{r,y}^\top m_{exo} g. \end{aligned} \quad (41)$$

Rearranging and simplifying (41) leads to

$$\alpha m_{exo} g (\hat{\mathbf{J}}_{r,y}^\top - \hat{\mathbf{J}}_{l,y}^\top) = \hat{\mathbf{J}}_{r,y}^\top (m_{exo} g - F_{r,y}) - \hat{\mathbf{J}}_{l,y}^\top F_{l,y}. \quad (42)$$

Assuming vertical acceleration is not significant, i.e.,  $m_{exo} g = F_{l,y} + F_{r,y}$  results in

$$\begin{aligned} \alpha (F_{l,y} + F_{r,y}) (\hat{\mathbf{J}}_{r,y}^\top - \hat{\mathbf{J}}_{l,y}^\top) &= F_{l,y} (\hat{\mathbf{J}}_{r,y}^\top - \hat{\mathbf{J}}_{l,y}^\top) \\ \Rightarrow \alpha &= \frac{F_{l,y}}{F_{l,y} + F_{r,y}}. \end{aligned} \quad (43)$$

## APPENDIX E

### SUPPLEMENTARY KINEMATIC DATA

Fig. 12 shows the joint positions observed during the transparency and haptic rendering conditions. In both conditions, similar joint trajectories were observed. However, during the haptic rendering trials, a significantly smaller range of motion was observed. This can be explained by the rendered torques due to the virtual spring and damper elements.

## ACKNOWLEDGMENT

The authors would like to thank Tim Haswell for his technical support on the hardware improvements of the ExoMotus-X2 exoskeleton and Lorenzo Vianello for his help with the experimentation. Presented data will be available upon request.

## REFERENCES

- [1] J. C. Moreno, J. Figueiredo, and J. L. Pons, *Chapter 7 - Exoskeletons for Lower-Limb Rehabilitation*. Amsterdam, The Netherlands: Elsevier, 2018.
- [2] W. Huo, S. Mohammed, J. C. Moreno, and Y. Amirat, “Lower limb wearable robots for assistance and rehabilitation: A state of the art,” *IEEE Syst. J.*, vol. 10, no. 3, pp. 1068–1081, Sep. 2016.
- [3] G. S. Sawicki, O. N. Beck, I. Kang, and A. J. Young, “The exoskeleton expansion: Improving walking and running economy,” *J. NeuroEng. Rehabil.*, vol. 17, no. 1, pp. 1–9, 2020.

- [4] L. M.-Crespo, P. Tsangaridis, D. Obwesgeser, S. Maggioni, and R. Riener, "Haptic error modulation outperforms visual error amplification when learning a modified gait pattern," *Front Neurosci*, vol. 13, Feb. 2019, Art. no. 61.
- [5] H.-J. Lee et al., "A wearable hip assist robot can improve gait function and cardiopulmonary metabolic efficiency in elderly adults," *IEEE Trans. Neural Syst. Rehabil. Eng.*, vol. 25, no. 9, pp. 1549–1557, Sep. 2017.
- [6] B. Hobbs and P. Artermiadis, "A review of robot-assisted lower-limb stroke therapy: Unexplored paths and future directions in gait rehabilitation," *Front. Neurorobot.*, vol. 14, 2020, Art. no. 19.
- [7] R. Baud, A. R. Manzoori, A. Ijspeert, and M. Bouri, "Review of control strategies for lower-limb exoskeletons to assist gait," *J. NeuroEng. Rehabil.*, vol. 18, no. 1, Jul. 2021, Art. no. 119.
- [8] L. M.-Crespo and D. J. Reinkensmeyer, "Review of control strategies for robotic movement training after neurologic injury," *J. NeuroEng. Rehabil.*, vol. 6, no. 1, pp. 6–20, 2009.
- [9] G. Colombo et al., "Treadmill training of paraplegic patients using a robotic orthosis," *J. Rehabil. Res. Develop.*, vol. 37, no. 6, pp. 693–700, 2000.
- [10] S. K. Banala, S. K. Agrawal, and J. P. Scholz, "Active leg exoskeleton (ALEX) for gait rehabilitation of motor-impaired patients," in *Proc. IEEE 10th Int. Conf. Rehabil. Robot.*, 2007, pp. 401–407.
- [11] J. F. Veneman, R. Kruidhof, E. E. G. Hekman, R. Ekkelenkamp, E. H. F. V. Asseldonk, and H. v. d. Kooij, "Design and evaluation of the LOPES exoskeleton robot for interactive gait rehabilitation," *IEEE Trans. Neural Syst. Rehabil. Eng.*, vol. 15, no. 3, pp. 379–386, Sep. 2007.
- [12] S. A. Murray, K. H. Ha, C. Hartigan, and M. Goldfarb, "An assistive control approach for a lower-limb exoskeleton to facilitate recovery of walking following stroke," *IEEE Trans. Neural Syst. Rehabil. Eng.*, vol. 23, no. 3, pp. 441–449, May 2015.
- [13] A. Tsukahara et al., "Effects of gait support in patients with spinocerebellar degeneration by a wearable robot based on synchronization control," *J. NeuroEng. Rehabil.*, vol. 15, no. 1, Sep. 2018, Art. no. 84.
- [14] L. J. Mayag, M. Múnera, and C. A. Cifuentes, "Human-in-the-loop control for a GoRA unilateral lower-limb exoskeleton," *J. Intell. Robotic Systems: Theory Appl.*, vol. 104, no. 1, 2022, Art. no. 3.
- [15] C. Camardella, F. Porcini, A. Filippeschi, S. Marcheschi, M. Solazzi, and A. Frisoli, "Gait phases blended control for enhancing transparency on lower-limb exoskeletons," *IEEE Robot. Autom. Lett.*, vol. 6, no. 3, pp. 5453–5460, Jul. 2021.
- [16] J. Vantilt et al., "Model-based control for exoskeletons with series elastic actuators evaluated on sit-to-stand movements," *J. NeuroEng. Rehabil.*, vol. 16, no. 1, Jun. 2019, Art. no. 65.
- [17] R. M. Andrade, S. Sapienza, and P. Bonato, "Development of a 'transparent operation mode' for a lower-limb exoskeleton designed for children with cerebral palsy," in *Proc. IEEE Int. Conf. Rehabil. Robot.*, 2019, pp. 512–517.
- [18] R. M. Andrade, S. Sapienza, E. E. Fabara, and P. Bonato, "Trajectory tracking impedance controller in 6-DoF lower-limb exoskeleton for over-ground walking training: Preliminary results," in *Proc. IEEE Int. Symp. Med. Robot.*, 2021, pp. 1–6.
- [19] Y. Tu et al., "An adaptive sliding mode variable admittance control method for lower limb rehabilitation exoskeleton robot," *Appl. Sci.*, vol. 10, no. 7, 2020, Art. no. 2536.
- [20] M. Sharifi, J. K. Mehr, V. K. Mushahwar, and M. Tavakoli, "Adaptive CPG-based gait planning with learning-based torque estimation and control for exoskeletons," *IEEE Robot. Autom. Lett.*, vol. 6, no. 4, pp. 8261–8268, Oct. 2021.
- [21] H. Kazerooni, R. Steger, and L. Huang, "Hybrid control of the Berkeley lower extremity exoskeleton (BLEEX)," *Int. J. Robot. Res.*, vol. 25, no. 5/6, pp. 561–573, 2006.
- [22] J. C. Moreno, N. Vitiello, C. Walsh, H. Huang, and S. Mohammed, "Introduction to the special section on wearable robots," *IEEE Trans. Robot.*, vol. 38, no. 3, pp. 1338–1342, Jun. 2022.
- [23] R. M. Andrade and P. Bonato, "The role played by mass, friction, and inertia on the driving torques of lower-limb gait training exoskeletons," *IEEE Trans. Med. Robot. Bionics*, vol. 3, no. 1, pp. 125–136, Feb. 2021.
- [24] D. Zanotto, T. Lenzi, P. Stegall, and S. K. Agrawal, "Improving transparency of powered exoskeletons using force/torque sensors on the supporting cuffs," in *Proc. IEEE 13th Int. Conf. Rehabil. Robot.*, 2013, pp. 1–6.
- [25] W. v. Dijk, H. v. d. Kooij, B. Koopman, E. H. F. v. Asseldonk, and H. v. d. Kooij, "Improving the transparency of a rehabilitation robot by exploiting the cyclic behaviour of walking," in *Proc. IEEE 13th Int. Conf. Rehabil. Robot.*, 2013, pp. 1–8.
- [26] J. Pratt, P. Dilworth, and G. Pratt, "Virtual model control of a bipedal walking robot," in *Proc. Int. Conf. Robot. Autom.*, 1997, pp. 193–198.
- [27] M. Mistry, J. Buchli, and S. Schaal, "Inverse dynamics control of floating base systems using orthogonal decomposition," in *Proc. IEEE Int. Conf. Robot. Autom.*, 2010, pp. 3406–3412.
- [28] J. Vantilt, C. Giraddi, E. Aertbeliën, F. D. Groote, and J. D. Schutter, "Estimating contact forces and moments for walking robots and exoskeletons using complementary energy methods," *IEEE Robot. Autom. Lett.*, vol. 3, no. 4, pp. 3410–3417, Oct. 2018.
- [29] M. J. Claros, R. Soto, J. L. Gordillo, J. L. Pons, and J. L. C.-Vidal, "Robotic assistance of human motion using active-backdrivability on a geared electromagnetic motor," *Int. J. Adv. Robotic Syst.*, vol. 13, no. 2, pp. 1–10, 2016.
- [30] J. Fong et al., "CANopen robot controller (CORC): An open software stack for human robot interaction development," in *Proc. Int. Symp. Wearable Robot.*, 2020, pp. 287–292.
- [31] L. Li, Z. Xie, X. Luo, and J. Li, "Effects of torso pitch motion on energy efficiency of biped robot walking," *Appl. Sci.*, vol. 11, no. 5, 2021, Art. no. 2342.
- [32] B. Hwang and D. Jeon, "A method to accurately estimate the muscular torques of human wearing exoskeletons by torque sensors," *Sensors*, vol. 15, no. 4, pp. 8337–8357, 2015.
- [33] J. Barkley Rosser, "Nine-point difference solutions for Poisson's equation," *Comput. Math. Appl.*, vol. 1, no. 3, pp. 351–360, 1975.
- [34] M. Fumagalli and R. Carloni, "A modified impedance control for physical interaction of UAVs," in *Proc. IEEE Int. Conf. Intell. Robots Syst.*, 2013, pp. 1979–1984.
- [35] Y. Zimmermann, E. B. Kucuktanak, F. Farshidian, R. Riener, and M. Hutter, "Towards dynamic transparency : Robust interaction force tracking using multi-sensory control on an arm exoskeleton," in *Proc. IEEE/RSJ Int. Conf. Intell. Robots Syst.*, 2020 pp. 7417–7424.
- [36] B. Stellato, G. Banjac, P. Goulart, A. Bemporad, and S. Boyd, "OSQP: An operator splitting solver for quadratic programs," *Math. Program. Computation*, vol. 12, no. 4, pp. 637–672, 2020.
- [37] C. D. Bellicoso, C. Gehring, J. Hwangbo, P. Fankhauser, and M. Hutter, "Perception-less terrain adaptation through whole body control and hierarchical optimization," in *Proc. IEEE-RAS Int. Conf. Humanoid Robots*, 2016, pp. 558–564.
- [38] Y. Zimmermann, A. Forino, R. Riener, and M. Hutter, "ANYExo: A versatile and dynamic upper-limb rehabilitation robot," *IEEE Robot. Autom. Lett.*, vol. 4, no. 4, pp. 3649–3656, Oct. 2019.
- [39] S.-Y. Jang, J.-H. Youn, S. H. Lim, S. S. Kim, U. Kim, and K.-U. Kyung, "Development of a three-axis monolithic flexure-based ground reaction force sensor for various gait analysis," *IEEE Robot. Autom. Lett.*, vol. 7, no. 2, pp. 4118–4125, Apr. 2022.
- [40] R. Gehlhar, J.-H. Yang, and A. D. Ames, "Powered prosthesis locomotion on varying terrains: Model-dependent control with real-time force sensing," *IEEE Robot. Autom. Lett.*, vol. 7, no. 2, pp. 5151–5158, Apr. 2022.
- [41] D. A. Revi, A. M. Alvarez, C. J. Walsh, S. M. De Rossi, and L. N. Awad, "Indirect measurement of anterior-posterior ground reaction forces using a minimal set of wearable inertial sensors: From healthy to hemiparetic walking," *J. NeuroEng. Rehabil.*, vol. 17, no. 1, Jun. 2020, Art. no. 82.
- [42] Y. Wen, J. Si, A. Brandt, X. Gao, and H. H. Huang, "Online reinforcement learning control for the personalization of a robotic knee prosthesis," *IEEE Trans. Cybern.*, vol. 50, no. 6, pp. 2346–2356, Jun. 2020.
- [43] E. B. Küçüktanak, S. J. Kim, Y. Wen, K. Lynch, and J. L. Pons, "Human-machine-human interaction in motor control and rehabilitation: A review," *J. NeuroEng. Rehabil.*, vol. 18, no. 1, Dec. 2021, Art. no. 183.
- [44] S. J. Kim et al., "A framework for dyadic physical interaction studies during ankle motor tasks," *IEEE Robot. Autom. Lett.*, vol. 6, no. 4, pp. 6876–6883, Oct. 2021.
- [45] S. J. Kim et al., "Effect of dyadic haptic collaboration on ankle motor learning and task performance," *IEEE Trans. Neural Syst. Rehabil. Eng.*, vol. 31, pp. 416–425, Feb. 2022.



**Emek Barış Küçüktabak** (Student Member, IEEE) received the B.S. degree from Middle East Technical University, Ankara, Turkey, in 2017, and the M.S. degree from ETH Zurich, Zurich, Switzerland, in 2019, both in mechanical engineering. Currently, he is working toward the Ph.D. degree with the Center for Robotics and Biosystems, Northwestern University, Evanston, IL, USA, and with the Legs+Walking Lab, the Shirley Ryan AbilityLab, Chicago, IL.

His research interests include physical human–robot interaction, teleoperation, force control, and assistive robotics.



**Yue Wen** received the B.S. degree in automation from Wuhan University of Technology, Wuhan, China, in 2011, the M.S. degree in control theory and engineering from Huazhong University of Science and Technology, Wuhan, in 2014, and the Ph.D. degree in biomedical engineering from North Carolina State University Raleigh, NC, USA, and the University of North Carolina at Chapel Hill, Chapel Hill, NC, in 2019.

He is currently an Assistant Professor with the Department of Mechanical and Aerospace Engineering, University of Central Florida, Orlando, FL, USA. His research interests include the control and personalization of wearable robots, deep learning for neural machine interfaces, human–robot interaction, and gait rehabilitation.



**Sangjoon J. Kim** received the B.S. degree from the Department of Electrical and Computer Engineering, the University of Wisconsin-Madison, Madison, WI, USA, in 2012. He received the M.S. and Ph.D. degrees, both in mechanical engineering, from the Korea Advanced Institute of Science and Technology, Daejeon, South Korea, in 2014 and 2019, respectively.

He is currently an Assistant Project Scientist with the University of California-Irvine, Irvine, CA, USA, concurrently holding a position as a Research Engineer with Flint Rehabilitation, Irvine. His research interests primarily focus on biomedical engineering and robotics.



**Matthew R. Short** received the B.S. degree in bioengineering from Temple University, Philadelphia, PA, USA, in 2018. He is currently working toward the Ph.D. degree with Northwestern University, Chicago, IL, USA, working with the Neurorehabilitation and Neural Engineering Lab, Shirley Ryan AbilityLab, Chicago.

His research interests include human–human interaction and ankle motor control in the context of poststroke rehabilitation.



**Daniel Ludvig** (Member, IEEE) received the B.Sc. degree in physiology and physics in 2003, and the M.Eng. and Ph.D. degrees in biomedical engineering, in 2006 and 2010, respectively, all from McGill University, Montreal, QC, Canada.

He is currently a Research Assistant Professor with the Department of Biomedical Engineering, Northwestern University, Evanston, IL, USA, and a Research Scientist with the Shirley Ryan AbilityLab in Chicago, IL. He specializes in using quantitative and experimentally driven techniques to model human biomechanics and motor control. His current specific research interests include quantifying the role lower-limb neuromechanics play in healthy locomotion, and how alterations in these neuromechanics lead to injury and disease.



**Levi Hargrove** (Member, IEEE) received the M.Sc.E. and Ph.D. degrees in electrical engineering from the University of New Brunswick, Fredericton, Canada, in 2005 and 2008, respectively.

He is currently the Director and Scientific Chair with Center for Bionic Medicine, the Shirley Ryan AbilityLab, Chicago, IL, USA, and an Associate Professor with the Departments of Physical Medicine and Rehabilitation and the McCormick School of Engineering, Northwestern University, Evanston, IL, USA. His research interests include signal processing, pattern recognition, and control of bionic limbs.



**Eric J. Perreault** received the B.S. and M.S. degrees in electrical engineering from McGill University, Montreal, PQ, Canada, in 1989 and 1992, respectively, and the Ph.D. degree in biomedical engineering from Case Western Reserve University, Cleveland, OH, USA, in 2000.

He is Vice President for Research and Professor of biomedical engineering and physical medicine and rehabilitation with Northwestern University, Evanston, IL, USA. His research interests focus on the neural and biomechanical factors involved in the control of multijoint movement and posture and how they are modified following neuromotor pathologies, such as stroke and spinal cord injury.

Dr. Perreault is a Fellow of the American Institute for Medical and Biological Engineering, and was recently the Chair of the National Advisory Board on Medical Rehabilitation Research, and the President of the International Society for Electrophysiology and Kinesiology.



**Kevin M. Lynch** (Fellow, IEEE) received the B.S.E. degree in electrical engineering from Princeton University, Princeton, NJ, USA, in 1989, and the Ph.D. degree in robotics from Carnegie Mellon University, Pittsburgh, PA, USA, in 1996.

He is a Professor of mechanical engineering with Northwestern University, Chicago, IL, USA, where he directs the Center for Robotics and Biosystems and is a Member of the Northwestern Institute on Complex Systems. He is a coauthor of the textbooks *Principles of Robot Motion* (Cambridge, MA, USA: MIT Press, 2005) and *Modern Robotics: Mechanics, Planning, and Control* (Cambridge, U.K.: Cambridge Univ. Press, 2017) and the associated online courses and videos. His research interests include robot manipulation and locomotion, self-organizing multiagent systems, and physically collaborative human–robot systems.



**José L. Pons** (Senior Member, IEEE) received the graduation degree in mechanical engineering from Universidad de Navarra, Pamplona, Spain, in 1992, and the M.Sc. degree in information technologies from Universidad Politécnica de Madrid, Madrid, Spain, in 1994, and the Ph.D. degree in physics from Universidad Complutense de Madrid, Madrid, in 1997, for his research work on dynamic optimization of robot mechanisms.

He currently is the Scientific Chair with the Legs + Walking AbilityLab, Shirley Ryan AbilityLab, Chicago, IL, USA. In addition to the research leadership role with SRAlab, he holds appointments as Professor with the Department of Physical Medicine and Rehabilitation, Feinberg School of Medicine, Chicago, and with the Departments of Biomedical Engineering and Mechanical Engineering, McCormick School of Engineering, Northwestern University, Evanston, IL, USA.